



TOI 4201 b and TOI 5344 b: Discovery of Two Transiting Giant Planets around M-dwarf Stars and Revised Parameters for Three Others

J. D. Hartman¹ , G. Á. Bakos¹ , Z. Csabry¹, A. W. Howard² , H. Isaacson³ , S. Giacalone³ , A. Chontos¹ , N. Narita^{4,5,6} , A. Fukui^{4,6} , J. P. de Leon⁷ , N. Watanabe⁷ , M. Mori⁷ , T. Kagetani⁷ , I. Fukuda⁷ , Y. Kawai⁷ , M. Ikoma⁸ , E. Palle^{6,9} , F. Murgas^{6,9} , E. Esparza-Borges^{6,9} , H. Parviainen^{6,9} , L. G. Bouma² , M. Cointepas^{10,11} , X. Bonfils¹⁰ , J. M. Almenara¹¹ , Karen A. Collins¹² , Kevin I. Collins¹³ , Howard M. Relles¹² , Khalid Barkaoui^{6,14,15} , Richard P. Schwarz¹² , Ghachoui Mourad^{14,16} , Mathilde Timmermans¹⁴, Georgina Dransfield¹⁷, Artem Burdanov¹⁸ , Julien de Wit¹⁸ , Emmanuël Jehin¹⁹ , Amaury H. M. J. Triaud¹⁷ , Michaël Gillon¹⁴ , Zouhair Benkhaldoun¹⁶ , Keith Horne²⁰ , Ramotholo Sefako²¹ , A. Jordán^{22,23,24,25} , R. Brahm^{22,23,24} , V. Suc^{22,25} , Steve B. Howell²⁶ , E. Furlan²⁷ , J. E. Schlieder²⁸ , D. Ciardi²⁷ , T. Barclay²⁸ , E. J. Gonzales²⁹ , I. Crossfield³⁰ , C. D. Dressing³ , M. Goliguzova³¹ , A. Tatarnikov³¹ , George R. Ricker³² , Roland Vanderspek³² , David W. Latham¹² , S. Seager^{32,33,34} , Joshua N. Winn¹ , Jon M. Jenkins²⁶ , Stephanie Striegel^{26,35} , Avi Shporer³² , Andrew Vanderburg³² , Alan M. Levine³² , Veselin B. Kostov^{28,35} , and David Watanabe³⁶

¹ Department of Astrophysical Sciences, Princeton University, 4 Ivy Lane, Princeton, NJ 08544, USA; jhartman@astro.princeton.edu

² Department of Astronomy, California Institute of Technology, Pasadena, CA 91125, USA

³ Department of Astronomy, University of California at Berkeley, Berkeley, CA 94720, USA

⁴ Komaba Institute for Science, The University of Tokyo, 3-8-1 Komaba, Meguro, Tokyo 153-8902, Japan

⁵ Astrobiology Center, 2-21-1 Osawa, Mitaka, Tokyo 181-8588, Japan

⁶ Instituto de Astrofísica de Canarias (IAC), E-38200 La Laguna, Tenerife, Spain

⁷ Department of Multi-disciplinary Sciences, Graduate School of Arts and Sciences, The University of Tokyo, 3-8-1 Komaba, Meguro, Tokyo 153-8902, Japan

⁸ Division of Science, National Astronomical Observatory of Japan, 2-21-1 Osawa, Mitaka, Tokyo 181-8588, Japan

⁹ Departamento de Astrofísica, Universidad de La Laguna (ULL), E-38206 La Laguna, Tenerife, Spain

¹⁰ Univ. Grenoble Alpes, CNRS, IPAG, F-38000 Grenoble, France

¹¹ Observatoire de Genève, Département d'Astronomie, Université de Genève, Chemin Pegasi 51b, 1290 Versoix, Switzerland

¹² Center for Astrophysics | Harvard & Smithsonian, 60 Garden Street, Cambridge, MA 02138, USA

¹³ George Mason University, 4400 University Drive, Fairfax, VA 22030 USA

¹⁴ Astrobiology Research Unit, Université de Liège, 19C Allée du 6 Août, B-4000 Liège, Belgium

¹⁵ Department of Earth, Atmospheric and Planetary Science, Massachusetts Institute of Technology, 77 Massachusetts Avenue, Cambridge, MA 02139, USA

¹⁶ Oukaimeden Observatory, ¹⁷ High Energy Physics and Astrophysics Laboratory, Faculty of sciences Semlalia, Cadi Ayyad University, Marrakech, Morocco

¹⁸ School of Physics & Astronomy, University of Birmingham, Edgbaston, Birmingham B15 2TT, UK

¹⁹ Department of Earth, Atmospheric and Planetary Sciences, MIT, 77 Massachusetts Avenue, Cambridge, MA 02139, USA

²⁰ Space Sciences, Technologies and Astrophysics Research (STAR) Institute, Université de Liège, Allée du 6 Août 19C, B-4000 Liège, Belgium

²¹ SUPA School of Physics and Astronomy, University of St Andrews, North Haugh, St Andrews KY16 9SS, Scotland, UK

²² South African Astronomical Observatory, P.O. Box 9, Observatory, Cape Town 7935, South Africa

²³ Facultad de Ingeniería y Ciencias, Universidad Adolfo Ibáñez, Av. Diagonal las Torres 2640, Peñalolén, Santiago, Chile

²⁴ Millennium Institute for Astrophysics, Chile

²⁵ Data Observatory Foundation, Chile

²⁶ El Sauce Observatory—Obstech, Chile

²⁷ NASA Ames Research Center, Moffett Field, CA 94035, USA

²⁸ NASA Exoplanet Science Institute, Caltech/IPAC, Mail Code 100-22, 1200 E. California Boulevard, Pasadena, CA 91125, USA

²⁹ NASA Goddard Space Flight Center, 8800 Greenbelt Road, Greenbelt, MD 20771, USA

³⁰ Department of Astronomy and Astrophysics, University of California Santa Cruz, Santa Cruz, CA 95064, USA

³¹ Department of Physics & Astronomy, University of Kansas, Lawrence, KS 66045, USA

³² Sternberg Astronomical Institute, Lomonosov Moscow State University, Universitetskii, 13, Moscow, Russia

³³ Department of Physics and Kavli Institute for Astrophysics and Space Research, Massachusetts Institute of Technology, Cambridge, MA 02139, USA

³⁴ Department of Earth, Atmospheric and Planetary Sciences, Massachusetts Institute of Technology, Cambridge, MA 02139, USA

³⁵ Department of Aeronautics and Astronautics, MIT, 77 Massachusetts Avenue, Cambridge, MA 02139, USA

³⁶ SETI Institute, 189 Bernardo Ave., Suite 200, Mountain View, CA 94043, USA

³⁷ Planetary Discoveries in Valencia, CA 91354, USA

Received 2023 July 13; revised 2023 August 24; accepted 2023 August 29; published 2023 October 3

Abstract

We present the discovery from the TESS mission of two giant planets transiting M-dwarf stars: TOI 4201 b and TOI 5344 b. We also provide precise radial velocity measurements and updated system parameters for three other M dwarfs with transiting giant planets: TOI 519, TOI 3629, and TOI 3714. We measure planetary masses of $0.525 \pm 0.064 M_J$, $0.243 \pm 0.020 M_J$, $0.689 \pm 0.030 M_J$, $2.57 \pm 0.15 M_J$, and $0.412 \pm 0.040 M_J$ for TOI 519 b, TOI 3629 b, TOI 3714 b, TOI 4201 b, and TOI 5344 b, respectively. The corresponding stellar masses are $0.372 \pm 0.018 M_\odot$, $0.635 \pm 0.032 M_\odot$, $0.522 \pm 0.028 M_\odot$, $0.626 \pm 0.033 M_\odot$, and $0.612 \pm 0.034 M_\odot$. All five hosts have supersolar metallicities, providing further support for recent findings that, like for solar-type stars, close-in giant



Original content from this work may be used under the terms of the [Creative Commons Attribution 4.0 licence](https://creativecommons.org/licenses/by/4.0/). Any further distribution of this work must maintain attribution to the author(s) and the title of the work, journal citation and DOI.

planets are preferentially found around metal-rich M-dwarf host stars. Finally, we describe a procedure for accounting for systematic errors in stellar evolution models when those models are included directly in fitting a transiting planet system.

Unified Astronomy Thesaurus concepts: [Exoplanet systems \(484\)](#)

1. Introduction

M-dwarf stars are the most common type of star in the Galaxy, making up approximately 70% of the local stellar population (Henry et al. 2018). These stars often host short-period Earth-size planets (Dressing & Charbonneau 2015), but they are not expected to be common hosts of giant planets. Theoretical predictions based on the core accretion model of planet formation suggest that the occurrence rate of giant planets around $0.5 M_{\odot}$ stars is only 10% that of giant planets around G dwarfs and that it drops to essentially zero for stars with masses less than $\sim 0.4 M_{\odot}$ (Burn et al. 2021). However, other work by Mercer & Stamatellos (2020) has indicated that the formation of giant planets via gravitational instabilities may actually be enhanced around M dwarfs.

The vast majority of stars currently known to host giant planets have F, G, or K spectral types. Based on the NASA Exoplanet Archive (NASA Exoplanet Archive 2023),³⁷ only 18 of the 733 giant planets with $M_p \sin i > 0.1 M_J$ discovered to date by the radial velocity (RV) method orbit M-dwarf stars,³⁸ and only 16 of the 621 confirmed giant planets discovered to date by the transit method orbit M dwarfs. The low representation of M-dwarf hosts within the current sample of giant planets suggests that giant planets are not common around M dwarfs. However, such observations can be misleading because the current sample derives from surveys that are biased toward solar-type host stars.

Statistical analyses of early RV surveys found hints that the occurrence rate of giant planets is indeed smaller for M dwarfs than for solar-type stars (Johnson et al. 2010), but the small sample size left large uncertainties on the occurrence estimate. More recently, Sabotta et al. (2021) and Pass et al. (2023) have reported, based on RV surveys, occurrence rates for giant planets around M dwarfs that are below that for solar-mass host stars. Occurrence rates for giant planets around M dwarfs have also been determined from observations by the NASA TESS mission (Ricker et al. 2015) by Bryant et al. (2023) and Gan et al. (2023), with these limits being focused on much shorter period planets ($P < 10$ days) than the RV surveys, which are often sensitive out to $P \sim 1000$ days. Bryant et al. (2023) find an occurrence rate of $0.194\% \pm 0.072\%$ for close-in giant planets around M dwarfs, while Gan et al. (2023) find a rate of $0.27\% \pm 0.09\%$. The rate of hot Jupiters around M dwarfs thus appears to be lower than the rate for solar-type stars by a factor of ~ 2.5 – 5 . For mid- to late M dwarfs, the rate is still $\gtrsim 0.1\%$, which is perhaps larger than theoretical predictions.

The very large population of M dwarfs in the Galaxy, coupled with a giant planet occurrence rate that is small but not vanishingly small, means that there should be a substantial number of giant planets hosted by such stars. Assuming that the occurrence rate of giant planets around M dwarfs is $1/5$ that of giant planets around G stars, we might expect $\sim 1/3$ of giant

planets in the Galaxy to orbit M dwarfs, whereas only 2%–3% of the existing sample of giant planets have M-dwarf hosts.

Finding this missing population of giant planets around M dwarfs would not only allow for a better determination of the occurrence rate of these planets, and thus better tests of planet formation theories; it would also create better opportunities to characterize the physical properties of a poorly studied class of exoplanets. This could include leveraging the very deep transits of giant planets that transit M dwarfs to study the atmospheres of these planets via transmission spectroscopy (Charbonneau et al. 2002), or leveraging starspot crossing events in transiting systems to measure the obliquities of the stellar hosts in these systems (e.g., Sanchis-Ojeda & Winn 2011). To date no such studies have been published for the currently small sample of giant planets known to transit M dwarfs.

In recent years there has been an increase in the rate of finding giant planets around M dwarfs. This increase is due in part to RV surveys focused on M dwarfs (Reiners et al. 2018), as well as transiting systems discovered by Kepler (Johnson et al. 2012), HATSouth (Hartman et al. 2015; Bakos et al. 2018; Jordán et al. 2022), NGTS (Bayliss et al. 2018), and TESS (Cañas et al. 2020; Artigau et al. 2021; Kanodia et al. 2021; Parviainen et al. 2021; Gan et al. 2022; Cañas et al. 2022; Hobson et al. 2023; Kanodia et al. 2022, 2023). Key factors contributing to the recent yield of such systems have been the development of IR-sensitive high-precision RV instruments (e.g., Tamura et al. 2012; Artigau et al. 2014; Quirrenbach et al. 2014); transit surveys that cover a larger number of faint M-dwarf stars compared to earlier surveys; efforts to use RV instruments on large telescopes, such as Keck I/HIRES, VLT/ESPRESSO, Subaru/IRD, and Magellan/PFS, to provide RV confirmation of candidate transiting giant planets around these faint M dwarfs; and the development of instruments capable of simultaneous, multiband, time-series photometry.

In this paper we present the discovery of two new transiting giant planets around M-dwarf stars by the TESS mission: TOI 4201 b and TOI 5344 b. These planets were identified by TESS, followed up with a variety of ground-based photometric time-series facilities, and confirmed via precise RV observations with Keck I/HIRES. We also present new Keck I/HIRES RV observations for three other previously confirmed transiting giant planets around M-dwarf stars designated as TOI 519 (Parviainen et al. 2021), TOI 3629, and TOI 3714 (Cañas et al. 2022). We combine the new RVs with new photometric time-series observations presented here and with previously published observations to update the physical parameters for these three systems.

In analyzing these systems, we follow a typical method of utilizing theoretical stellar evolution models to constrain the properties of the host stars. This method can yield higher-precision parameter values than purely empirical techniques; however, it can also lead to parameter constraints that are much tighter than systematic errors in the evolution models themselves (e.g., Tayar et al. 2022; Hobson et al. 2023). Systematic uncertainties are often reported along with the statistical uncertainties (Hobson et al. 2023), but sometimes the

³⁷ Accessed on 2023-06-22 at 14:16.

³⁸ For the purposes of this discussion we take M dwarfs to be stars with $T_{\text{eff}} < 4000$ K, which may include late K dwarfs as well.

Table 1
Summary of Photometric Observations

Instrument/Field ^a	Date(s)	No. of Images ^b	Cadence ^c (s)	Filter	Precision ^d (mmag)
TOI 519					
TESS/Sector 7	2019 Jan–2019 Feb	16,240	120	<i>T</i>	32.1
TESS/Sector 34	2021 Jan–2021 Feb	16,835	120	<i>T</i>	21.5
TESS/Sector 61	2023 Jan–2023 Feb	15,453	120	<i>T</i>	21.4
CHAT 0.7 m	2019 Mar 24	31	258	<i>i</i>	7.3
LCOGT 1.0 m	2019 Mar 29	108	86	<i>g'</i>	20.4
LCOGT 1.0 m	2019 Apr 1	53	176	<i>i'</i>	7.0
LCOGT 1.0 m	2019 Apr 16	51	176	<i>B</i>	26.9
LCOGT 1.0 m	2019 Apr 16	77	176	<i>z_s</i>	4.3
MuSCAT2	2019 Nov 23	166	63	<i>g</i>	19.4
MuSCAT2	2019 Nov 23	166	63	<i>r</i>	9.4
MuSCAT2	2019 Nov 23	166	63	<i>i</i>	5.9
MuSCAT2	2019 Nov 23	166	63	<i>z_s</i>	5.2
MuSCAT2	2020 Jan 9	118	63	<i>g</i>	56.5
MuSCAT2	2020 Jan 9	116	63	<i>r</i>	16.8
MuSCAT2	2020 Jan 9	119	63	<i>i</i>	8.3
MuSCAT2	2020 Jan 9	118	63	<i>z_s</i>	6.2
MuSCAT2	2020 Jan 14	130	63	<i>g</i>	53.9
MuSCAT2	2020 Jan 14	131	63	<i>r</i>	16.3
MuSCAT2	2020 Jan 14	131	63	<i>i</i>	8.0
MuSCAT2	2020 Jan 14	131	63	<i>z_s</i>	4.7
MuSCAT2	2020 Feb 29	525	16	<i>g</i>	60.2
MuSCAT2	2020 Feb 29	137	60	<i>r</i>	11.8
MuSCAT2	2020 Feb 29	138	60	<i>i</i>	7.5
MuSCAT2	2020 Feb 29	137	60	<i>z_s</i>	6.2
ExTrA—tel2	2021 Jan 30	164	62	0.85–1.55 μm	15.5
ExTrA—tel3	2021 Jan 30	163	62	0.85–1.55 μm	11.8
ExTrA—tel2	2021 Feb 9	178	62	0.85–1.55 μm	18.6
ExTrA—tel3	2021 Feb 9	179	62	0.85–1.55 μm	13.4
ExTrA—tel2	2021 Mar 4	188	62	0.85–1.55 μm	12.1
ExTrA—tel3	2021 Mar 4	189	62	0.85–1.55 μm	11.5
ExTrA—tel2	2021 Mar 9	149	62	0.85–1.55 μm	11.5
ExTrA—tel3	2021 Mar 9	147	62	0.85–1.55 μm	11.6
ExTrA—tel2	2021 Mar 23	190	62	0.85–1.55 μm	14.9
ExTrA—tel3	2021 Mar 23	191	62	0.85–1.55 μm	12.2
ExTrA—tel2	2021 Apr 16	186	62	0.85–1.55 μm	16.9
MuSCAT2	2022 Mar 19	150	91	<i>r</i>	25.5
MuSCAT2	2022 Mar 19	152	91	<i>z_s</i>	7.2
TOI 3629					
TESS/Sector 17	2019 Oct 9–31	693	1800	<i>T</i>	2.0
TESS/Sector 57	2022 Sep–2022 Oct	17,966	120	<i>T</i>	5.9
LCOGT 1.0 m	2021 Oct 17	244	90	<i>i'</i>	1.7
MuSCAT2	2021 Oct 25	176	60	<i>g</i>	4.4
MuSCAT2	2021 Oct 25	215	51	<i>r</i>	2.9
MuSCAT2	2021 Oct 25	677	16	<i>i</i>	3.9
MuSCAT2	2021 Oct 25	420	26	<i>z_s</i>	3.2
TOI 3714					
TESS/Sector 19	2019 Nov–2019 Dec	812	1800	<i>T</i>	3.9
MuSCAT2	2021 Aug 28	96	91	<i>g</i>	46.1
MuSCAT2	2021 Aug 28	100	91	<i>i</i>	19.5
MuSCAT2	2021 Aug 28	72	91	<i>z_s</i>	20.6
MuSCAT3/LCOGT 2.0 m	2021 Sep 3	35	303	<i>g'</i>	1.6
MuSCAT3/LCOGT 2.0 m	2021 Sep 3	98	111	<i>r'</i>	2.0
MuSCAT3/LCOGT 2.0 m	2021 Sep 3	186	59	<i>i'</i>	1.9
MuSCAT3/LCOGT 2.0 m	2021 Sep 3	184	60	<i>z_s</i>	1.6
MuSCAT2	2021 Sep 25	422	35	<i>g</i>	8.6
MuSCAT2	2021 Sep 25	214	71	<i>r</i>	4.6
MuSCAT2	2021 Sep 25	577	26	<i>i</i>	4.0
MuSCAT2	2021 Sep 25	581	26	<i>z_s</i>	3.7
TRAPPIST-North	2022 Sep 21	256	70	<i>I + z</i>	3.1
SPECULOOS-North	2022 Oct 19	149	130	<i>g'</i>	4.0
SPECULOOS-North	2022 Oct 30	222	67	<i>r'</i>	3.3

Table 1
(Continued)

Instrument/Field ^a	Date(s)	No. of Images ^b	Cadence ^c (s)	Filter	Precision ^d (mmag)
TRAPPIST-North	2022 Oct 30	160	100	<i>z</i>	3.5
TOI 4201					
TESS/Sector 6	2018 Dec–2019 Jan	977	1800	<i>T</i>	8.7
LCOGT 1.0 m	2021 Sep 26	23	545	<i>g'</i>	9.1
LCOGT 1.0 m	2021 Sep 26	24	545	<i>i'</i>	6.5
LCOGT 1.0 m	2021 Oct 3	26	546	<i>g'</i>	3.7
LCOGT 1.0 m	2021 Oct 3	25	546	<i>i'</i>	4.2
MuSCAT	2022 Jan 30	124	121	<i>g</i>	3.7
MuSCAT	2022 Jan 30	300	51	<i>r</i>	2.4
MuSCAT	2022 Jan 30	298	51	<i>z</i>	2.0
ExTrA—tel2	2022 Nov 2	162	62	0.85–1.55 μm	6.5
ExTrA—tel1	2022 Dec 15	152	62	0.85–1.55 μm	5.5
ExTrA—tel2	2022 Dec 15	152	62	0.85–1.55 μm	6.5
ExTrA—tel3	2022 Dec 15	152	62	0.85–1.55 μm	6.5
ExTrA—tel3	2023 Jan 20	210	62	0.85–1.55 μm	7.1
SPECULOOS-North	2023 Feb 24	513	30	<i>z'</i>	3.9
ExTrA—tel1	2023 Mar 4	184	62	0.85–1.55 μm	6.6
ExTrA—tel2	2023 Mar 4	182	62	0.85–1.55 μm	7.8
ExTrA—tel3	2023 Mar 4	184	62	0.85–1.55 μm	10.1
TOI 5344					
TESS/Sector 43	2021 Sep–2021 Oct	2815	600	<i>T</i>	7.5
TESS/Sector 44	2021 Oct–2021 Nov	2756	600	<i>T</i>	6.0
LCOGT 0.4 m	2022 Mar 1	26	417	<i>i'</i>	4.6
TRAPPIST-North	2022 Aug 26	150	80	<i>I + z</i>	3.1
ExTrA—tel1	2022 Dec 15	161	62	0.85–1.55 μm	5.1
ExTrA—tel2	2022 Dec 15	160	62	0.85–1.55 μm	4.8
ExTrA—tel3	2022 Dec 15	161	62	0.85–1.55 μm	4.7
MuSCAT2	2022 Dec 18	341	41	<i>g</i>	7.7
MuSCAT2	2022 Dec 18	340	41	<i>r</i>	4.5
MuSCAT2	2022 Dec 18	649	21	<i>i</i>	4.8
MuSCAT2	2022 Dec 18	652	21	<i>z_s</i>	5.3
SPECULOOS-North	2023 Jan 6	108	170	<i>g'</i>	4.0
ExTrA—tel2	2023 Jan 22	103	62	0.85–1.55 μm	5.8
ExTrA—tel3	2023 Jan 22	102	62	0.85–1.55 μm	5.1

Notes.^a For TESS data we list the sector from which the observations are taken.^b Excluding any outliers or other data not included in the modeling.^c The median time between consecutive images rounded to the nearest second. Due to factors such as weather, the day–night cycle, guiding, and focus corrections, the cadence is only approximately uniform over short timescales.^d The rms of the residuals from the best-fit model. Note that in the case of TESS observations the transit may appear artificially shallower owing to overfiltering and/or blending from unresolved neighbors. As a result, the S/N of the transit may be less than what would be calculated from R_p/R_* and the rms estimates given here.

systematic uncertainties are overestimates for parameters with empirical constraints, such as the mean stellar density (Eastman et al. 2023). In this paper we also describe a method for incorporating systematic errors in stellar evolution models into the analysis of transiting planet systems in a manner that self-consistently allows for tighter empirical constraints on parameters when available.

In Section 2 we discuss the observations that are used to confirm and characterize each planetary system. In Section 3 we describe the analysis methods. In Section 4 we discuss the results.

2. Observations

All five of the systems presented here were first detected as transiting planet candidates based on observations by the

NASA TESS mission. Additional ground-based light curves and high-precision RV measurements were gathered for each system and combined with catalog astrometric and photometric data to determine the parameters of the system (Section 3). Three of the systems discussed here (TOI 519, TOI 3629, and TOI 3714) have already been studied in the literature. For these systems we briefly describe the published data that we employed and then describe our new RV observations and light curves. For the two systems that are new discoveries (TOI 4201 and TOI 5344) we describe in greater detail the space-based and ground-based light curves, as well as the RV observations used to confirm the objects as transiting planet systems. The light curves used in the analysis of each system are summarized in Table 1, while the RV data are summarized in Table 2. Identifying information for the five systems are given in Tables 3 and 4.

Table 2
Summary of Radial Velocity Observations

Instrument	UT Date(s)	No. of Spec.	S/N Range ^a	RV Precision ^b (m s ⁻¹)	Source
TOI 519					
Subaru/IRD	2021 May 4–2022 Jan 24	18	...	42	Kagetani et al. (2023)
Keck I/HIRES	2021 October 26	1	44	...	this paper
Keck I/HIRES+I ₂	2021 Nov 19–2022 Jan 8	7	24–57	70	this paper
TOI 3629					
Hobby-Eberly/HPF	2021 Jan 18–2022 Jan 14	23	...	18	Cañas et al. (2022)
WIYN 3.5 m/NEID	2021 Sep 21–2021 Nov 28	5	...	13	Cañas et al. (2022)
Keck I/HIRES	2022 Jun 7	1	100	...	this paper
Keck I/HIRES+I ₂	2022 Aug 11–2022 Sep 18	9	68–77	16	this paper
TOI 3714					
Hobby-Eberly/HPF	2021 Aug 24–2021 Dec 23	12	...	33	Cañas et al. (2022)
Keck I/HIRES+I ₂	2021 Sep 21	1	71	...	this paper
WIYN 3.5 m/NEID	2021 Sep 22–2022 Jan 8	8	...	11	Cañas et al. (2022)
Keck I/HIRES+I ₂	2021 Sep 24–2021 Nov 28	7	47–70	18	this paper
TOI 4201					
Keck I/HIRES	2022 Sep 7	1	66	...	this paper
Keck I/HIRES+I ₂	2022 Sep 9–2023 Jan 10	12	50–71	41	this paper
TOI 5344					
Keck I/HIRES+I ₂	2022 Sep 1–2023 Jan 10	13	55–71	15	this paper
Keck I/HIRES	2022 Sep 7	1	68	1	this paper

Notes.

^a S/N from the exposure meter for the Keck I/HIRES observation.

^b The scatter in the RV residuals from the best-fit orbit, which may include astrophysical jitter. We do not have an RV precision estimate for the Keck I/HIRES template I₂-free template observations.

2.1. TOI 519

Parviainen et al. (2021) announced the discovery of TOI 519 b, and Kagetani et al. (2023) published a mass measurement for the planet based on Subaru/IRD RV measurements. Transits of this system were first detected in the Sector 7 observations from TESS. The TESS observations were obtained at 120 s cadence and reduced to trend-filtered light curves by the NASA Science Processing Operations Center (SPOC) Pipeline at NASA Ames Research Center (Jenkins et al. 2010, 2016). Multiple threshold crossing events were detected, and the target passed all of the data validation tests conducted by the pipeline. The Sector 7 light curve was combined with a variety of multiband ground-based light curves to rule out a stellar mass companion to TOI 519. Here we combine the light curves that were previously used by Parviainen et al. (2021) with new RV observations from Keck I/HIRES to determine the parameters of the system.

2.1.1. High-contrast Imaging

High-contrast imaging observations to search for resolved stellar companions of TOI 519 have been reported on ExoFOP-TESS,³⁹ but they were not included in Parviainen et al. (2021). These observations include adaptive optics (AO) imaging in the *K* band with the NIRC2 instrument on the Keck II 10 m telescope on the night of 2019 April 7, speckle imaging at 692 nm and 880 nm with the DSSI instrument on the LDT 4.3 m telescope on 2020 February 10, and speckle imaging at 562 and 832 nm with the Álopeke instrument on the Gemini 8 m telescope on the night of 2020 February 18. No companions were detected in any of these observations. The LDT/DSSI observations were reported in Clark et al. (2022).

The NIRC2 observations and reductions followed the approach described by Schlieder et al. (2021). The estimated point-spread function width of the resulting image is 0''103, and a contrast of $\Delta K = 7.742$ mag at 0''5 separation is achieved. For the Álopeke observations, data were reduced as described in Howell et al. (2011), and the 5σ contrast achieved is $\Delta m = 4.86$ mag at 0''5 for the 832 nm observation and $\Delta m = 4.01$ mag at 0''5 for the 562 nm observation.

2.1.2. Light Curves

In addition to the 120 s cadence TESS light curve from Sector 7 that was produced by SPOC and included in the analysis of Parviainen et al. (2021), TOI 519 was also observed by TESS at 120 s cadence during Sectors 34 and 61, as well as at a cadence of 30 minutes via the full-frame images (FFIs) gathered during Sector 8. We obtained the 120 s cadence SPOC light curves from MAST for the three relevant sectors, while for Sector 8 an FFI light curve for this source was not publicly available, so we do not include those data in the analysis. We used the Pre-search Data Conditioning (PDC) light curves from the SPOC project (Stumpe et al. 2014; Smith et al. 2012; Stumpe et al. 2012).

Ground-based follow-up light curves of TOI 519 obtained with the Las Cumbres Observatory Global Telescope (LCOGT) 1 m network (Brown et al. 2013) and with the MuSCAT2 multicolor imager (Narita et al. 2019) on the 1.52 m Telescopio Carlos Sánchez (TCS) at Teide Observatory have all been presented and discussed by Parviainen et al. (2021), who made these data available to us.

A light curve of TOI 519 was obtained with the Chilean-Hungarian Automated Telescope (CHAT) 0.7 m telescope at Las Campanas Observatory in Chile. These observations were carried out through an *i*-band filter on the night of 2019 March

³⁹ <https://exofop.ipac.caltech.edu/tess/index.php>

24 and were reduced to trend-filtered light curves following Jordán et al. (2019).

A total of six distinct transit events of TOI 519 b were observed with the Exoplanets in Transits and their Atmospheres (ExTrA) facility (Bonfils et al. 2015). Five of the events were observed by two of the three 0.6 m ExTrA telescopes, leading to a total of 11 independent transit light curves from ExTrA that we include in the analysis of this system. Spectrophotometric observations were carried out over a wavelength range of 0.85–1.55 μm and were reduced to light curves integrated over the full bandpass following Cointepas et al. (2021).

An additional transit of TOI 519 b was observed in r and z_s bands on 2022 March 19 with MuSCAT2. These data were reduced to light curves following Parviainen et al. (2020).

2.1.3. Radial Velocities

We obtained Keck I/HIRES (Vogt et al. 1994) observations of TOI 519 between 2021 October 26 and 2022 January 08. A total of seven observations were obtained through the I_2 cell, together with a single I_2 -free template exposure. Observations were carried out through the California Planet Search (CPS; Howard et al. 2010; Howard & Fulton 2016) queue and were made using the C2 decker, with an exposure time of 900 s. The seeing ranged between 0".9 and 1".7, and the total counts recorded by the HIRES exposure meter for each observation were between 600 and 3200.

The HIRES spectra were reduced to relative RV measurements and corrected for barycentric motion following standard CPS procedures. Spectral-line bisector span (BS) measurements were determined following Torres et al. (2007). The data are included in Table 5 and plotted in Figure 1.

Kagetani et al. (2023) published 18 RVs of TOI 519 derived from mid-IR spectra obtained with Subaru/IRD (Tamura et al. 2012; Kotani et al. 2018). We incorporated these RV measurements into our joint analysis of this system.

2.2. TOI 3629

TOI 3629 was identified as a transiting planet candidate by Cañas et al. (2022), who carried out a custom reduction of the 30-minute-cadence TESS observations performed during Sector 17 of the mission. This object was also independently selected as a transiting planet candidate by the TESS Quick Look Pipeline (QLP; Huang et al. 2020). TOI 3629 was also confirmed as a transiting planet by Cañas et al. (2022) based on RV observations with the Habitable-zone Planet Finder (HPF; Mahadevan et al. 2012, 2014) and NEID (Halverson et al. 2016; Schwab et al. 2016) spectrographs.

We obtained Keck I/HIRES observations of TOI 3629. Here we combine the light curves and RVs for this system from Cañas et al. (2022) with the new Keck I/HIRES RVs, an additional sector of TESS observations, and a set of ground-based light curves not analyzed by Cañas et al. (2022) to update the parameters for the system.

2.2.1. High-contrast Imaging

High-contrast imaging of TOI 3629 was reported by Cañas et al. (2022), who ruled out bright companions with a magnitude difference $\Delta m < 4$ at separations between 0".2 and 1".2 from TOI 3629.

2.2.2. Light Curves

We make use of the 30-minute-cadence TESS Sector 17 light curve of TOI 3629 produced by the QLP and made accessible on MAST. For our analysis we use the detrended time series denoted with the keyword KSPSAP (i.e., it was produced through the Kepler Spline Simple Aperture Photometry method). In addition to the Sector 17 observations, TOI 3629 was also observed at 120 s cadence during Sector 57 of the TESS mission. We make use of the PDC light curve produced by SPOC from these data, which we obtained from MAST.

Ground-based follow-up light curves of TOI 3629 have been made available on the ExoFOP-TESS archive maintained by the NASA Exoplanet Archive at IPAC. None of these light curves were previously included in the analysis of Cañas et al. (2022), so we describe these here. We do not include light curves that did not cover the transit event in this discussion.

An ingress was observed in i' with the SINISTRO imager on one of the LCOGT 1 m telescopes at Teide Observatory, in Spain, on the night of 2021 October 17. Light curves were derived from these observations using ASTROIMAGEJ (Collins et al. 2017).

A full transit of TOI 3629 was observed using the MuSCAT2 imager on the 1.52 m TCS on the night of 2021 October 24. Observations were performed simultaneously in g , r , i , and z_s . Light curves were produced from the observations in a similar fashion to TOI 519 (Section 2.1.2).

While we restrict our analysis to the light curves discussed above, we note that Cañas et al. (2022) presented additional follow-up transit light curves of TOI 3629 from the RBO 0.6 m telescope and the 1.55 m Kuiper Telescope.

2.2.3. Radial Velocities

Cañas et al. (2022) published RV observations of TOI 3629 from HPF and NEID. These include a total of 23 HPF RVs obtained between 2021 January 18 and 2022 January 14 and 5 NEID RVs obtained between 2021 September 21 and November 28. We included these published RVs in the reanalysis of the system presented in Section 3.

We carried out spectroscopic observations of TOI 3629 with Keck I/HIRES between 2022 June 07 and September 18. A total of nine spectra were gathered through the I_2 cell, and a single I_2 -free template spectrum was also obtained. Observations were made through the C2 decker, with seeing between 0".9 and 1".3. The template spectrum had an exposure time of 1200 s, while most of the I_2 -in observations had exposure times of 900 s. Two of the I_2 -in observations had shorter exposure times of 748 and 796 s. The exposure meter recorded between 4600 and 10,000 counts during each observation. The observations were reduced to high-precision RVs and BS measurements following the same methods as discussed for TOI 519.

2.3. TOI 3714

TOI 3714 was selected as a candidate transiting planet system by the QLP project based on 30-minute-cadence TESS FFI observations carried out in Sector 19. Like TOI 3629, TOI 3714 was also previously confirmed by Cañas et al. (2022) based on HPF and NEID RVs. We independently observed TOI 3714 with Keck I/HIRES. Here we revise the parameters for this system by combining the data from Cañas et al. (2022) with the new RVs.

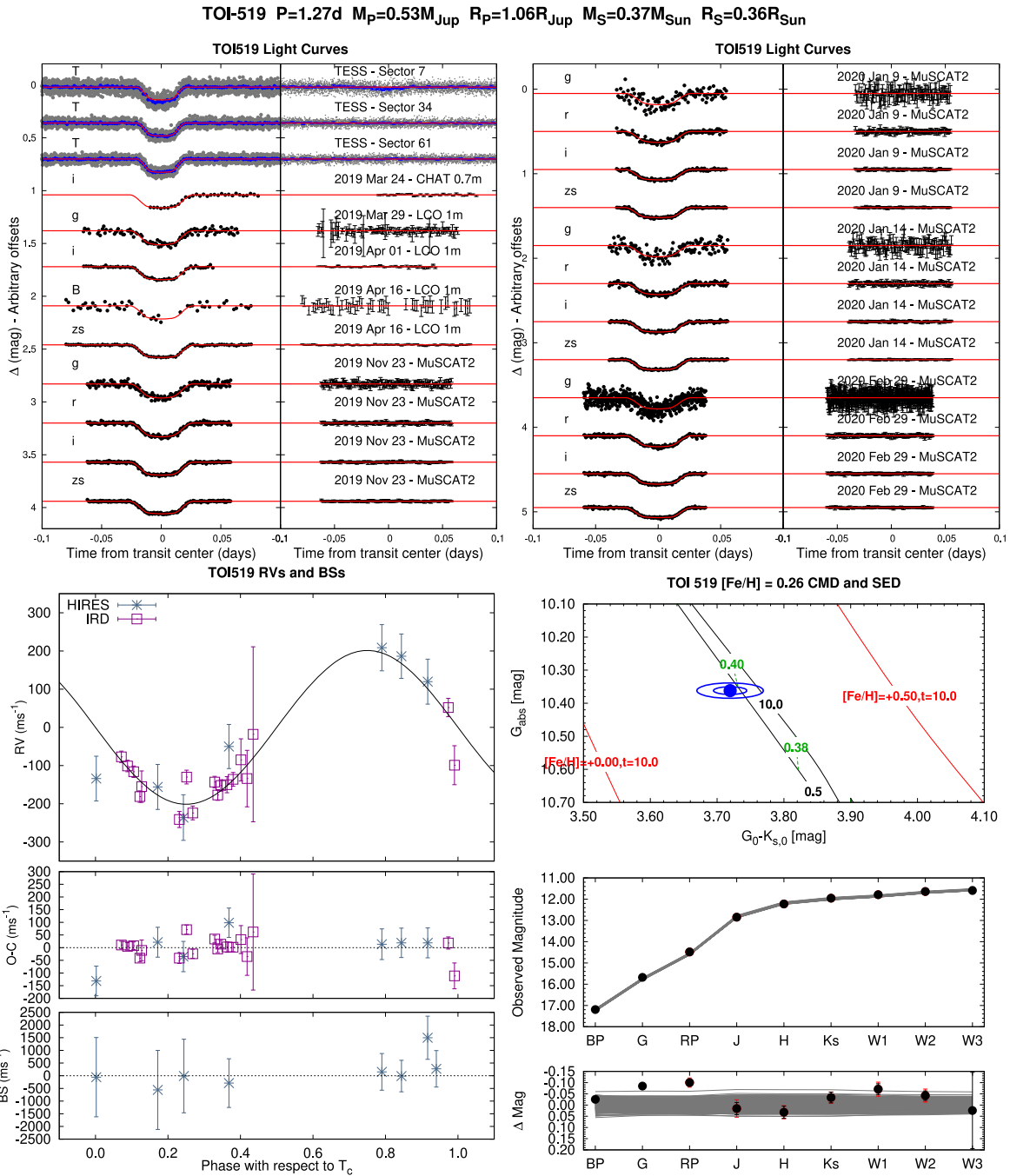


Figure 1. Observations incorporated into the analysis of the transiting planet system TOI 519. Top: transit light curves, with fitted model overplotted. The dates, filters, and instruments used are indicated. Additional light curves for this system are shown in Figure 3. For TESS we phase-fold the data and plot the unbinned observations in gray, with the phase-binned values overplotted in blue. The residuals for each light curve are shown on the right-hand side in the same order as the original light curves. The error bars represent the photon and background shot noise, plus the readout noise. Note that these uncertainties are increased by a common factor in the fitting procedure to achieve a reduced χ^2 of unity, but the uncertainties shown in the plot have not been scaled. Bottom left: high-precision RVs phased with respect to the mid-transit time. The top panel shows the phased measurements together with the best-fit model. The center-of-mass velocity has been subtracted. The middle panel shows the velocity $O - C$ residuals. The error bars include the estimated jitter, which is varied as a free parameter in the fitting. The bottom panel shows the spectral-line BSs. Bottom right: color–magnitude diagram (CMD) and spectral energy distribution (SED). The top panel shows the absolute G magnitude vs. the dereddened $G - K_s$ color compared to theoretical isochrones (black lines) and stellar evolution tracks (green lines) from the MIST models interpolated at the best-estimate value for the metallicity of the host. The age of each isochrone is listed in black in Gyr, while the mass of each evolution track is listed in green in solar masses. The solid red lines show isochrones at higher and lower metallicities than the best-estimate value, with the metallicity and age in Gyr of each isochrone labeled on the plot. The filled blue circle shows the measured reddening- and distance-corrected values from Gaia DR2 and the Two Micron All Sky Survey (2MASS), while the blue lines indicate the 1σ and 2σ confidence regions, including the estimated systematic errors in the photometry. The middle panel shows the SED as measured via broadband photometry through the listed filters. Here we plot the observed magnitudes without correcting for distance or extinction. Overplotted are 200 model SEDs randomly selected from the MCMC posterior distribution produced through the global analysis (gray lines). The model makes use of the predicted absolute magnitudes in each bandpass from the MIST isochrones, the distance to the system (constrained largely via Gaia DR2), and extinction (constrained from the SED with a prior coming from the MWDUST 3D Galactic extinction model). The bottom panel shows the $O - C$ residuals from the best-fit model SED. The errors listed in the catalogs for the broadband photometry measurements are shown with black lines, while the errors including an assumed 0.02 mag systematic uncertainty, which is added in quadrature to the listed uncertainties, are shown with red lines. The latter uncertainties are what we use in the fit.

2.3.1. High-contrast Imaging

High-contrast imaging of TOI 3714 was reported by Cañas et al. (2022), who ruled out bright companions with $\Delta m < 4$ at separations between $0''.2$ and $1''.2$ from TOI 3714. TOI 3714, however, does have a white dwarf companion that is reported in Gaia DR3 (Gaia Collaboration et al. 2023) at a separation of $2''.67$, and with $\Delta G = 4.56$ relative to TOI 3714. Cañas et al. (2022) measure a mass of $\sim 1.07 M_{\odot}$ and a cooling age of ~ 2.4 Gyr for this white dwarf. They adopted this as the age of the TOI 3714 system.

2.3.2. Light Curves

At the time of our analysis the only TESS observations available for TOI 3714 were the Sector 19 FFI data. We made use of the QLP light curve derived from these data and available on MAST, and we used the KSPSAP detrended time series in our analysis.

An ingress of TOI 3714 was observed using the MUSCAT3 instrument (Narita et al. 2020) on the LCOGT 2.0 m telescope at Haleakala on the night of 2021 September 03. Observations were gathered simultaneously through g' , r' , i' , and z_s filters. The data reduction and differential photometry were performed using the pipeline described in Fukui et al. (2011).

An egress was observed using MuSCAT2 on 2021 August 28 through g , i , and z_s bands, while a full transit was observed with this instrument on 2021 September 25 in the g , r , i , and z_s bands. These data were reduced to light curves in a similar fashion to the MuSCAT2 observations of TOI 519.

Two full transits of TOI 3714 were observed on the nights of 2022 September 21 and 2022 October 30 using the 0.6 m TRAPPIST-North (TRANSiting Planets and Planetesimals Small Telescope, Jehin et al. 2011; Gillon et al. 2011; Barkaoui et al. 2019) telescope. The first night of observations was carried out in the $I+z$ band, while the observations on the second night were performed using a z -band filter. Observations were scheduled using the tools of Jensen (2013), and the data were reduced to light curves following Garcia et al. (2022).

Two full transits of TOI 3714 were observed using the SPECULOOS-North 1.0 m telescope (Delrez et al. 2018; Sebastian et al. 2021; Burdanov et al. 2022) and an Andor ikon-L imager on the nights of 2022 October 19 and 30. The first transit was observed in g' , while the second was observed in r . The observations were scheduled following Sebastian et al. (2021) and reduced to light curves following Murray et al. (2020) and Garcia et al. (2021, 2022).

In addition to the above transit observations, Cañas et al. (2022) also reported RBO 0.6 m observations of TOI 3714 on the nights of 2021 August 16 and 2021 November 19 and observations with the ARCTIC imager on the ARC 3.5 m telescope at Apache Point Observatory on the night of 2021 November 21. These data have not been published in an electronically accessible form, and we do not include them in our analysis of the system.

2.3.3. Radial Velocities

Cañas et al. (2022) published RV observations of TOI 3714 from HPF and NEID. These include a total of 12 HPF RVs obtained between 2021 August 24 and December 23 and 8 NEID RVs obtained between 2021 September 22 and 2022

January 01. We included these published RVs in the reanalysis of the system presented in Section 3.

We carried out spectroscopic observations of TOI 3714 with Keck I/HIRES between 2021 September 21 and November 28. A total of seven spectra were gathered through the I_2 cell, and a single I_2 -free template spectrum was also obtained. Observations were made through the C2 decker, with seeing between $1''.0$ and $1''.6$. The template spectrum had an exposure time of 619 s, while most of the I_2 -in observations had exposure times of 900 s. One of the I_2 -in observations had an exposure time of 945 s. The exposure meter recorded between 2200 and 5000 counts during each observation. The observations were reduced to high-precision RVs and BS measurements following the same methods as discussed for TOI 519 (Section 2.1.3).

2.4. TOI 4201

TOI 4201 was identified as a transiting planet candidate by QLP based on a search of the TESS FFI observations gathered during Sector 6 of the mission. The TESS Science Office (TSO) reviewed the vetting information and issued an alert on 2021 July 12 following the process described by Guerrero et al. (2021). Since confirmation of this object as a transiting planet has not yet been published, we describe all of the RV and photometric observations that we use to confirm the existence of this planet.

2.4.1. High-contrast Imaging

High-contrast speckle imaging was performed with the Zorro instrument on the Gemini 8 m telescope (Scott et al. 2021). Observations were obtained at 832 and 562 nm on 2023 April 24. The data were processed following the methods of Howell et al. (2011). No companions were detected, and contrast limits of 5.28 and 3.52 mag are achieved at separations greater than $0''.5$ in the 832 and 562 nm filters, respectively. Furthermore, no neighbors are listed within $10''$ of TOI 4201 in the Gaia DR3 catalog either.

2.4.2. Light Curves

We extracted an image-subtraction-based light curve from the TESS FFI Sector 6 observations of TOI 4201 following the methods of the CDIPS project (Bouma et al. 2019). We decorrelated against trends in the time series using a B-spline and then applied the TFA algorithm to filter additional systematic variations from the data.

TOI 4201 was observed by the LCOGT 1 m telescopes at Siding Spring Observatory (SSO), the South Africa Astronomical Observatory (SAAO), and Cerro Tololo Inter-American Observatory (CTIO) on the nights of 2021 September 1, 2021 September 26, and 2021 October 3, respectively. The first night was observed using an i' filter, while observations on the second and third nights were obtained using both i' and g' filters. Observations on the first night were out of transit, so we do not include these data in the analysis. The second night covered an ingress, while the third night covered a full transit event. These data were reduced to light curves using ASTRO-IMAGEJ (Collins et al. 2017).

A full transit of TOI 4201 was observed in z' on 2023 February 24 using the SPECULOOS-North 1 m telescope. These observations and reductions were carried out in a similar fashion to the SPECULOOS observations of TOI 3714 (Section 2.3.2).

A full transit was observed on 2022 January 30 in g , r , and z bands with MuSCAT (Narita et al. 2015). These were reduced to light curves in a similar fashion to the reduction of the MuSCAT3 observation of TOI 3714 (Section 2.3.2).

Transits were observed with the ExTrA facility on 2022 November 2, 2022 December 15, 2023 January 20, and 2023 March 4. A total of eight independent $0.85\text{--}1.55\ \mu\text{m}$ light curves were obtained with the various telescopes from this facility. The data were reduced in a similar manner to TOI 519 (Section 2.1.2).

2.4.3. Radial Velocities

We carried out spectroscopic observations of TOI 4201 with Keck I/HIRES between 2022 September 7 and 2023 January 10. A total of 12 exposures were taken through the I_2 cell, and a single I_2 -free template spectrum was also obtained. Observations were made through the C2 decker, with seeing between $1''.0$ and $1''.8$. The template spectrum had an exposure time of 1200 s, while the I_2 -in observations had exposure times between 900 and 1300 s. The exposure meter recorded between 2500 and 5000 counts during each observation. The observations were reduced to high-precision RVs and BS measurements following the same methods as discussed for TOI 519 (Section 2.1.3).

2.5. TOI 5344

TOI 5344 was identified as a transiting planet candidate by the QLP based on a search of the TESS FFI observations gathered for this target during Sectors 43 and 44 of the mission. The TSO reviewed the vetting information and issued an alert on 2022 February 28. Since confirmation of this object as a transiting planet has not yet been published, we describe all of the RV and photometric observations that we use to confirm the existence of the planet.

2.5.1. High-contrast Imaging

High-contrast speckle interferometric I -band imaging of TOI 5344 was obtained with the 2.5 m telescope at the Caucasian Observatory of Sternberg Astronomical Institute (SAI) of Lomonosov Moscow State University (Strakhov et al. 2023) on 2023 January 27. No companion is detected to a contrast limit of $\Delta I < 4$ mag at separations of $0''.2$ or more and $\Delta I < 7$ mag at separations of $1''$ or more.

2.5.2. Light Curves

We use the QLP light curves of TOI 5344 derived from the TESS FFI observations from Sectors 43 and 44 of the mission. We accessed these data from MAST and make use of the KSPSAP detrended time series for each sector.

A full transit of TOI 5344 was observed using the SBIG imager on the LCOGT 0.4 m telescope at Teide Observatory on the night of 2022 March 1. The observations were performed using an i' filter and were reduced to light curves using ASTROIMAGEJ (Collins et al. 2017).

A full transit was also observed using the TRAPPIST-North 0.6 m telescope and an $I+z$ filter on the night of 2022 August 26. Observations were scheduled and reduced in a similar manner to TRAPPIST-North observations of TOI 3714 (Section 2.3.2).

Two transits were observed with the ExTrA facility on 2022 December 15 and 2023 January 22. A total of five independent $0.85\text{--}1.55\ \mu\text{m}$ light curves were obtained with the various telescopes from this facility. The data were reduced in a similar fashion to TOI 519 (Section 2.1.2).

A full transit was observed with MuSCAT2 simultaneously in the g , r , i , and z_s bands on 2022 December 18. The observations were carried out and reduced in a similar manner to TOI 519 (Section 2.1.2).

Finally, a full transit was observed with the SPECULOOS-North 1.0 m telescope through a g' filter on 2023 June 6. The observations and reductions were carried out in a similar fashion to the SPECULOOS observations and reductions of TOI 3714 (Section 2.3.2).

2.5.3. Radial Velocities

We carried out spectroscopic observations of TOI 5344 with Keck I/HIRES between 2022 September 1 and 2023 January 10. A total of 13 exposures were taken through the I_2 cell, and a single I_2 -free template spectrum was also obtained. Observations were made through the C2 decker, with seeing between $0''.9$ and $1''.6$. The template spectrum had an exposure time of 1200 s, while the I_2 -in observations had exposure times between 900 and 1200 s. The exposure meter recorded between 3000 and 5000 counts during each observation. The observations were reduced to high-precision RVs and BS measurements following the same methods as discussed for TOI 519 (Section 2.1.3).

3. Analysis

3.1. Derivation of Stellar Atmospheric Parameters

The stellar atmospheric parameters $T_{\text{eff}\star}$ and $[\text{Fe}/\text{H}]$ were adopted or derived for each system as follows. We did not determine $v \sin i$ values for any of the stars studied here, as the processes used to determine the atmospheric parameters do not yield reliable $v \sin i$ values for M-dwarf stars. We visually confirm that none of the spectra show notable rotational broadening, from which we estimate an upper limit of $v \sin i \lesssim 10\ \text{km s}^{-1}$ for each system.

TOI 519: We applied the SpecMatch-Empirical procedure (Yee et al. 2017) to the I_2 -free template HIRES spectrum of TOI 519 to measure $T_{\text{eff}\star} = 3937 \pm 70\ \text{K}$ and $[\text{Fe}/\text{H}] = 0.390 \pm 0.090$. For comparison, Parviainen et al. (2021) list $T_{\text{eff}\star} = 3350 \pm 200\ \text{K}$. They obtained this value by determining a spectral type of M3.0–M4.5 based on a low-resolution spectrum from the Alhambra Faint Object Spectrograph and Camera (ALFOSC) on the Nordic Optical Telescope (NOT). This was then translated to an estimate of the effective temperature using the spectral type– $T_{\text{eff}\star}$ relation from Houdebine et al. (2019).

TOI 3629: We adopted $T_{\text{eff}\star} = 3870 \pm 90\ \text{K}$ and $[\text{Fe}/\text{H}] = 0.40 \pm 0.10$ from Cañas et al. (2022), who applied the HPF-SpecMatch package (Stefansson et al. 2020) to the HPF spectra of TOI 3629. For comparison, applying the SpecMatch-Empirical procedure to the I_2 -free template HIRES spectrum gives $T_{\text{eff}\star} = 3789 \pm 70\ \text{K}$ and $[\text{Fe}/\text{H}] = 0.48 \pm 0.09$, consistent with the HPF values.

TOI 3714: We adopted $T_{\text{eff}\star} = 3660 \pm 90\ \text{K}$ and $[\text{Fe}/\text{H}] = 0.10 \pm 0.10$ from Cañas et al. (2022), who measured these parameters for TOI 3714 in the same fashion as they did for TOI 3629. For comparison, applying the SpecMatch-Empirical

Table 3
Astrometric, Spectroscopic, and Photometric Parameters for Newly Discovered Systems TOI 4201 and TOI 5344

Parameter	TOI 4201 Value	TOI 5344 Value	Source
Astrometric properties and cross-identifications:			
2MASS-ID	06015391-1327410	04130384 + 2054550	
TIC-ID	95057860	16005254	
TOI-ID	4201	5344	
Gaia DR2-ID	2997312063605005056	52359538285081728	
R.A. (J2000)	06 ^h 01 ^m 53 ^s .9212	04 ^h 13 ^m 03 ^s .8474	Gaia DR3
Decl. (J2000)	-13°27'41"0292	+20°54'54"9086	Gaia DR3
$\mu_{R.A.}$ (mas yr ⁻¹)	11.731 ± 0.017	40.325 ± 0.028	Gaia DR3
$\mu_{Decl.}$ (mas yr ⁻¹)	6.053 ± 0.018	-22.194 ± 0.020	Gaia DR3
Parallax (mas)	5.291 ± 0.019	7.305 ± 0.023	Gaia DR3
Spectroscopic properties:			
$T_{\text{eff}\star}$ (K)	3937 ± 70	3367 ± 70	see Section 3.1
[Fe/H]	0.390 ± 0.090	0.390 ± 0.090	see Section 3.1
Photometric properties: ^a			
G (mag) ^b	14.4805 ± 0.0028	14.3186 ± 0.0028	Gaia DR3
BP (mag) ^b	15.4724 ± 0.0034	15.5037 ± 0.0037	Gaia DR3
RP (mag) ^b	13.4948 ± 0.0039	13.2419 ± 0.0039	Gaia DR3
B (mag)	16.70 ± 0.14	16.880 ± 0.069	APASS ^c
V (mag)	15.297 ± 0.024	15.275 ± 0.069	APASS ^c
g (mag)	16.001 ± 0.055	16.106 ± 0.055	APASS ^c
r (mag)	14.655 ± 0.064	14.622 ± 0.043	APASS ^c
i (mag)	13.911 ± 0.084	13.603 ± 0.062	APASS ^c
J (mag) ^d	12.258 ± 0.021	11.799 ± 0.021	2MASS
H (mag) ^d	11.564 ± 0.024	11.087 ± 0.022	2MASS
K_s (mag) ^d	11.368 ± 0.025	10.860 ± 0.018	2MASS
$W1$ (mag) ^e	11.272 ± 0.024	10.739 ± 0.024	WISE
$W2$ (mag) ^e	11.301 ± 0.021	10.728 ± 0.020	WISE
$W3$ (mag) ^e	11.28 ± 0.15	10.55 ± 0.11	WISE

Notes.

^a We only include in the table catalog magnitudes that were included in our analysis of each system.

^b The listed uncertainties for the Gaia DR3 photometry are taken from the catalog. For the analysis we assume an additional systematic uncertainty of 0.02 mag for each bandpass.

^c From APASS DR6 as listed in the UCAC 4 catalog (Zacharias et al. 2013).

^d From the 2MASS catalog (Skrutskie et al. 2006).

^e From the 2021 February 16 ALLWISE Data release of the WISE mission (Cutri et al. 2021).

procedure to the I₂-free template HIRES spectrum gives $T_{\text{eff}\star} = 3594 \pm 70$ K and $[\text{Fe}/\text{H}] = 0.12 \pm 0.09$, consistent with the HPF values.

TOI 4201: We applied the SpecMatch-Empirical procedure to the I₂-free template HIRES spectrum of TOI 4201 to measure $T_{\text{eff}\star} = 3937 \pm 70$ K and $[\text{Fe}/\text{H}] = 0.390 \pm 0.090$.

TOI 5344: We applied the SpecMatch-Empirical procedure to the I₂-free template HIRES spectrum of TOI 5344 to measure $T_{\text{eff}\star} = 3766 \pm 70$ K and $[\text{Fe}/\text{H}] = 0.390 \pm 0.090$.

3.2. Transiting Planet Modeling

We performed a joint analysis for each system of the light curves, RV observations, astrometric parallaxes, catalog broadband photometric measurements, and spectroscopic atmospheric parameters (Tables 3 and 4). To do this, we followed the methods of Hartman et al. (2019) and Bakos et al. (2020), but with a significant modification to account for systematic errors in the theoretical stellar evolution models used in the fit. We discuss this modification in more detail below.

We model the light curves using the model of Mandel & Agol (2002), assuming a quadratic limb-darkening law for the host star. We vary the limb-darkening coefficients in the fit, with Gaussian priors based on the theoretical tabulations of

Claret et al. (2012, 2013) and Claret (2018). The RV observations are modeled assuming a Keplerian orbit. We use version 1.2 of the MIST theoretical stellar evolution models (Paxton et al. 2011, 2013, 2015; Choi et al. 2016; Dotter 2016) to model the broadband photometry and atmospheric parameters and to provide a constraint on the allowed combinations of the stellar bulk density, effective temperature, and metallicity. We also use the MWDUST 3D Galactic extinction model (Bovy et al. 2016) to place a Gaussian prior on the line-of-sight extinction A_V as a function of distance and to set a maximum allowed extinction. The extinction in each bandpass is calculated from A_V assuming an $R_V = 3.1$ law. For each system we perform an analysis assuming that the orbit is circular and a separate analysis allowing $\sqrt{e} \sin \omega$ and $\sqrt{e} \cos \omega$ to vary in the fit. A differential evolution Markov Chain Monte Carlo (MCMC) procedure is used to fit the observations and determine the uncertainties on the varied parameters (see Hartman et al. 2019, for a list of parameters and priors).

For M-dwarf stars, which have main-sequence lifetimes that exceed the current age of the Universe, the spread in the theoretical main sequence is typically much smaller than the observational uncertainties. As a result, using theoretical stellar evolution models in the joint analysis of a transiting planet system can lead to very small uncertainties on the stellar and

Table 4
Astrometric, Spectroscopic, and Photometric Parameters for Previously Discovered Systems TOI 519, TOI 3629, and TOI 3714

Parameter	TOI 519 Value	TOI 3629 Value	TOI 3714 Value	Source
Astrometric properties and cross-identifications:				
2MASS-ID	08182567–1939465	23591015 + 3918514	04381253 + 3927299	
TIC-ID	218795833	455784423	155867025	
TOI-ID	519	3629	3714	
Gaia DR2-ID	5707485527450614656	2881820324294985856	178924390478792320	
R.A. (J2000)	08 ^h 18 ^m 25 ^s .6680	23 ^h 59 ^m 10 ^s .3200	04 ^h 38 ^m 12 ^s .5354	Gaia DR3
Decl. (J2000)	−19°39′46″.5010	+39°18′51″.3200	+39°27′29″.9093	Gaia DR3
$\mu_{R.A.}$ (mas yr ^{−1})	−41.959 ± 0.029	185.707 ± 0.012	19.826 ± 0.025	Gaia DR3
$\mu_{Decl.}$ (mas yr ^{−1})	29.074 ± 0.027	1.010 ± 0.012	−70.762 ± 0.020	Gaia DR3
Parallax (mas)	8.681 ± 0.037	7.667 ± 0.017	8.838 ± 0.022	Gaia DR3
Spectroscopic properties:				
$T_{\text{eff}\star}$ (K)	3367 ± 70	3870 ± 90	3660 ± 90	see Section 3.1
[Fe/H]	−0.010 ± 0.090	0.40 ± 0.10	0.10 ± 0.10	see Section 3.1
Photometric properties: ^a				
G (mag) ^b	15.6770 ± 0.0028	13.8226 ± 0.0028	14.2908 ± 0.0028	Gaia DR3
BP (mag) ^b	17.1927 ± 0.0057	14.8939 ± 0.0031	15.5114 ± 0.0035	Gaia DR3
RP (mag) ^b	14.4819 ± 0.0039	12.7937 ± 0.0038	13.1948 ± 0.0039	Gaia DR3
B (mag)	16.093 ± 0.041	16.86 ± 0.13	APASS ^c	
V (mag)	14.639 ± 0.061	15.278 ± 0.020	APASS ^c	
g (mag)	15.380 ± 0.022	15.99 ± 0.18	APASS ^c	
r (mag)	14.055 ± 0.057	14.737 ± 0.011	APASS ^c	
i (mag)	13.111 ± 0.032	13.70 ± 0.14	APASS ^c	
J (mag) ^d	12.847 ± 0.027	11.424 ± 0.027	11.788 ± 0.020	2MASS
H (mag) ^d	12.226 ± 0.027	10.733 ± 0.030	11.109 ± 0.015	2MASS
K_s (mag) ^d	11.951 ± 0.024	10.553 ± 0.020	10.906 ± 0.017	2MASS
$W1$ (mag) ^e	11.790 ± 0.024	10.484 ± 0.022	10.779 ± 0.023	WISE
$W2$ (mag) ^e	11.642 ± 0.021	10.516 ± 0.020	10.744 ± 0.019	WISE
$W3$ (mag) ^e	11.59 ± 0.17	10.375 ± 0.067	10.546 ± 0.097	WISE

Notes.

^a We only include in the table catalog magnitudes that were included in our analysis of each system.

^b The listed uncertainties for the Gaia DR3 photometry are taken from the catalog. For the analysis we assume an additional systematic uncertainty of 0.02 mag for all bandpasses.

^c From APASS DR6 as listed in the UCAC 4 catalog (Zacharias et al. 2013).

^d From the 2MASS catalog (Skrutskie et al. 2006).

^e From the 2021 February 16 ALLWISE Data release of the WISE mission (Cutri et al. 2021).

planetary masses and radii, which are often well below the estimated systematic uncertainties in the evolution models themselves (Tayar et al. 2022; see also Hobson et al. 2023, for an example). As argued by Eastman et al. (2023), the uncertainties on the stellar masses and radii may be smaller than the estimates of Tayar et al. (2022) when using ρ_\star , as determined from the transit light curves, to self-consistently determine the other stellar parameters. The argument of Eastman et al. (2023) holds for a purely empirical determination of the system parameters; however, when theoretical stellar evolution models are used in constraining the fit to the observations, the systematic errors on the models must still be accounted for.

The key parameters that we vary in the fit that directly impact the stellar physical parameters are: (1) $T_{\text{eff}\star}$, (2) [Fe/H], (3) the square of the impact parameter b^2 , (4) ζ/R_\star , (5) R_p/R_\star , (6) $\sqrt{e} \cos \omega$, (7) $\sqrt{e} \sin \omega$, (8) $T_{c,0}$, and (9) $T_{c,N}$. Here $T_{c,0}$ is the time of transit center for some initial epoch, and $T_{c,N}$ is the time of transit center for a final epoch. Together $T_{c,0}$ and $T_{c,N}$ determine the orbital period. The parameter ζ/R_\star is the reciprocal of the half duration of the transit and is related to

a/R_\star by

$$\zeta/R_\star = a/R_\star \frac{2\pi(1 + e \sin \omega)}{P\sqrt{1 - b^2}\sqrt{1 - e^2}}. \quad (1)$$

Parameters (3)–(9) together determine ρ_\star , which is the parameter that is used, together with $T_{\text{eff}\star}$ and [Fe/H], to determine the stellar physical parameters via interpolation within a precomputed grid of MIST stellar evolutionary models. In addition to these parameters, the distance modulus μ and extinction A_V are also varied and are used to determine the predicted magnitude in each bandpass to be compared to the catalog magnitudes.

Here we augment the above parameters with four new systematic error parameters: $\Delta[\text{Fe}/\text{H}]_{\text{sys}}$, $\Delta T_{\text{eff},\text{sys}}$, $\Delta M_{\star,\text{sys}}$, and $\Delta M_{\text{bol},\text{sys}}$. Here $\Delta[\text{Fe}/\text{H}]_{\text{sys}}$ represents the systematic error on [Fe/H] in dex, $\Delta T_{\text{eff},\text{sys}}$ is the fractional systematic error in $T_{\text{eff}\star}$, $\Delta M_{\star,\text{sys}}$ is the fractional systematic error in M_\star , and $\Delta M_{\text{bol},\text{sys}}$ is the systematic error in the bolometric magnitude in units of magnitude. These act as hidden parameters that allow broader distributions in [Fe/H], $T_{\text{eff}\star}$, M_\star , and M_{bol} beyond

Table 5
 HIRES Relative Radial Velocities and Bisector Spans for TOI 519, TOI 3629, TOI 3714, TOI 4201, and TOI 5344

System	BJD (2,450,000+)	RV ^a (m s ⁻¹)	σ_{RV}^b (m s ⁻¹)	BS (m s ⁻¹)	σ_{BS} (m s ⁻¹)	Phase
TOI 519	9514.10954	272.5	717.8	0.940
TOI 519	9538.02709	186.28	19.67	-13.1	620.4	0.844
TOI 519	9543.01980	208.48	25.99	152.7	723.1	0.790
TOI 519	9545.01639	-50.05	18.86	-289.7	960.0	0.368
TOI 519	9546.03311	-155.93	21.90	-558.1	1558.5	0.172
TOI 519	9547.08385	-134.06	21.11	-57.3	1562.9	0.002
TOI 519	9565.95401	119.69	21.98	1498.4	850.2	0.917
TOI 519	9587.87529	-236.07	24.08	-10.4	1451.2	0.244
TOI 3629	9738.09644	0.0	147.1	0.303
TOI 3629	9803.11442	61.65	5.94	0.0	378.5	0.820
TOI 3629	9822.95907	23.33	4.06	0.861
TOI 3629	9827.06494	12.29	4.30	-61.9	148.5	0.904
TOI 3629	9831.96255	-28.53	4.59	2.1	259.3	0.148
TOI 3629	9833.99319	24.30	6.21	416.8	529.0	0.664
TOI 3629	9835.01084	-7.34	4.48	116.3	690.1	0.922
TOI 3629	9835.87585	-31.10	4.21	10.6	869.7	0.142
TOI 3629	9838.85563	12.97	3.86	-75.2	177.1	0.899
TOI 3629	9840.79082	-14.30	4.18	-122.8	228.9	0.391
TOI 3714	9479.00748	-904.2	649.4	0.307
TOI 3714	9481.98350	126.75	5.84	0.0	783.0	0.688
TOI 3714	9506.91898	-162.97	6.70	4173.0	1295.6	0.260
TOI 3714	9508.90928	-171.54	7.05	825.9	1581.3	0.184
TOI 3714	9513.94311	11.75	6.59	-2557.9	1283.5	0.520
TOI 3714	9537.93945	159.89	6.29	18.6	485.2	0.656
TOI 3714	9543.78921	-103.68	6.49	1551.1	631.4	0.371
TOI 3714	9547.11122	88.57	7.75	0.0	794.6	0.912
TOI 4201	9830.11551	262.9	619.0	0.448
TOI 4201	9832.09351	36.47	8.40	0.001
TOI 4201	9835.11032	413.78	7.00	0.843
TOI 4201	9890.00349	-333.41	11.29	0.168
TOI 4201	9891.02938	-174.50	6.63	-1048.0	1197.2	0.454
TOI 4201	9896.08512	345.02	7.33	-733.1	552.5	0.866
TOI 4201	9896.96372	-290.74	10.31	-1051.1	1155.6	0.111
TOI 4201	9897.93348	-385.68	7.83	-870.7	831.8	0.382
TOI 4201	9928.05123	468.67	8.06	259.0	760.1	0.790
TOI 4201	9943.90169	-436.74	6.84	-178.0	281.4	0.215
TOI 4201	9944.89630	-75.76	7.46	269.0	289.7	0.493
TOI 4201	9953.89179	-33.09	6.64	29.0	514.8	0.004
TOI 4201	9954.99279	-414.34	7.11	0.0	202.4	0.312
TOI 5344	9824.02822	-68.52	5.52	0.418
TOI 5344	9830.05085	-729.3	494.3	0.006
TOI 5344	9832.00717	6.71	5.95	0.522
TOI 5344	9834.07972	-29.60	5.18	0.069
TOI 5344	9835.07406	-45.75	5.03	-1709.3	1481.1	0.331
TOI 5344	9870.98245	70.01	5.06	135.2	277.5	0.799
TOI 5344	9889.95704	65.59	5.51	0.802
TOI 5344	9890.96999	-27.01	5.68	-589.5	320.9	0.069
TOI 5344	9897.81740	68.08	5.19	277.1	556.2	0.874
TOI 5344	9927.95984	85.65	6.03	227.0	361.7	0.822
TOI 5344	9943.85965	-10.02	5.42	163.1	387.4	0.014
TOI 5344	9944.91861	-72.49	6.29	56.8	602.7	0.293
TOI 5344	9953.84656	32.62	6.39	60.4	302.3	0.647
TOI 5344	9954.96159	29.88	8.25	-27.8	1339.0	0.941

Notes.

^a The zero-point of these velocities is arbitrary. An overall offset γ_{rel} fitted to the orbit has been subtracted for each system.

^b Internal errors excluding the component of astrophysical jitter allowed to vary in the fit.

what would be allowed by the stellar evolution model. The systematic error parameters are allowed to vary in the fit assuming Gaussian priors with mean values of 0 and standard

deviations of 0.08 dex, 0.024, 0.05, and 0.021 mag, respectively. These values for the systematic uncertainties are adopted from Tayar et al. (2022) and are based on current uncertainties

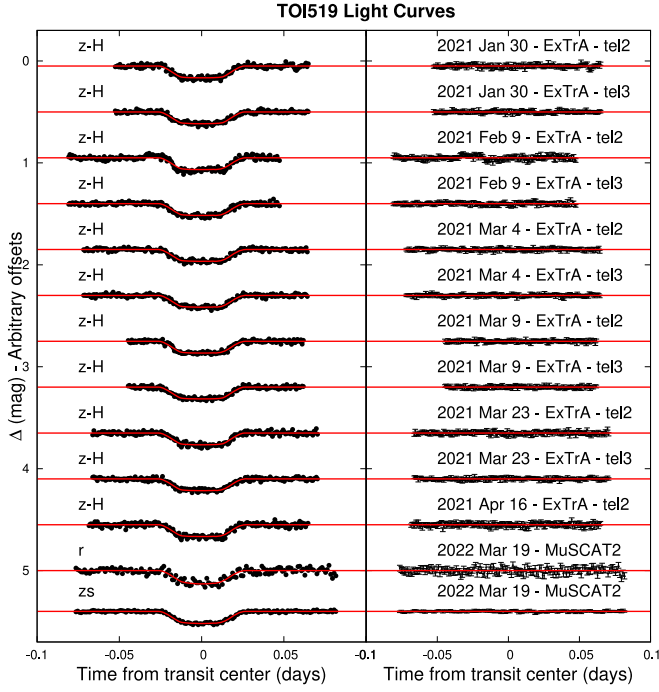


Figure 2. Additional light curves used in the analysis of TOI 519 displayed in the same manner as the other light curves shown in Figure 1.

on the measured interferometric angular diameters and bolometric fluxes of stars and comparisons between different grids of stellar evolution models.

Within each link in the Markov chain we take the combination of $(T_{\text{eff}\star}, [\text{Fe}/\text{H}], \rho_{\star}, \Delta[\text{Fe}/\text{H}]_{\text{sys}}, \Delta T_{\text{eff,sys}}, \text{ and } \Delta M_{\star,\text{sys}})$ and perform the look-up in the isochrone at the values $(T_{\text{eff}\star}(1 + \Delta T_{\text{eff,sys}}), [\text{Fe}/\text{H}] + \Delta[\text{Fe}/\text{H}]_{\text{sys}}, \rho_{\star})$. This yields the following set of predicted, isochrone-based, stellar parameters: $(M_{\star,\text{iso}}, R_{\star,\text{iso}}, L_{\star,\text{iso}}, \log g_{\star,\text{iso}}, V_{\text{mag,iso}}, T_{\text{eff,iso}})$.

We then correct the predicted, isochrone-based, stellar parameters for $\Delta M_{\star,\text{sys}}$ and $\Delta T_{\text{eff,sys}}$ to obtain the adopted parameters as follows:

$$M_{\star,\text{adopted}} = (1.0 + \Delta M_{\star,\text{sys}})M_{\text{star,iso}} \quad (2)$$

$$R_{\star,\text{adopted}} = (1.0 + \Delta M_{\star,\text{sys}})^{1/3}R_{\text{star,iso}} \quad (3)$$

$$\log L_{\star,\text{adopted}} = \log L_{\star,\text{iso}} + \frac{2}{3} \log(1.0 + \Delta M_{\star,\text{sys}}) + 4.0(\log(T_{\text{eff}\star}) - \log(T_{\text{eff,iso}})) \quad (4)$$

$$\log g_{\star,\text{adopted}} = \log g_{\star,\text{iso}} + \frac{1}{3} \log(1.0 + \Delta M_{\star,\text{sys}}) \quad (5)$$

$$V_{\text{mag,adopted}} = V_{\text{mag,iso}} - \frac{5}{3} \log(1.0 + \Delta M_{\star,\text{sys}}) - 10(\log(T_{\text{eff}\star}) - \log(T_{\text{eff,iso}})) \quad (6)$$

$$T_{\text{eff,adopted}} = T_{\text{eff}\star} \quad (7)$$

The adopted values are used to calculate the posterior distributions for the various stellar parameters. To account for $\Delta M_{\text{bol,sys}}$, we add this parameter to the predicted magnitudes in each filter before determining χ^2 for the model. Here $\Delta M_{\text{bol,sys}}$ accounts for the systematic uncertainty in calculating the bolometric magnitude from the theoretical luminosity of the star.

This procedure forces the model to have ρ_{\star} equal to the value determined from the transit parameters but allows M_{\star} and R_{\star} to differ from the values predicted from the theoretical stellar evolution model. Because we adjust the values for $L_{\star,\text{adopted}}$ and the associated magnitudes accordingly, it is possible that the measured catalog photometry and parallax values will constrain R_{\star} , and thus M_{\star} (through ρ_{\star}), to better than what one would calculate simply from the a priori systematic uncertainty on M_{\star} . The method that we employ here is able to self-consistently handle both systematic uncertainties present in stellar models and the full set of observations that might provide empirical constraints that are tighter than those systematic uncertainties. One limitation to our approach is that this procedure assumes that $\Delta T_{\text{eff,sys}}$, $\Delta M_{\star,\text{sys}}$, $\Delta[\text{Fe}/\text{H}]_{\text{sys}}$, and $\Delta M_{\text{bol,sys}}$ are uncorrelated, whereas the systematic errors in the stellar evolution models may very well be strongly correlated.

Figures 1–6 compares the best-fit models to the observational data. The adopted stellar parameters are listed in Tables 6 and 7, while the adopted planetary parameters are listed in Tables 8 and 9.

4. Discussion

In this paper we have presented the discovery of two new transiting giant planets that orbit M-dwarf stars and have updated the parameters for three other systems with new RVs and light curves. The system parameters are compared to the parameters of other transiting planet systems from the NASA Exoplanet Archive in Figures 7 and 8. Here the planet equilibrium temperature T_{eq} is calculated assuming zero albedo and full redistribution of heat, making it effectively a proxy for the incoming flux from the star at the orbital distance of the planet. We find that, like other giant planets found around M dwarfs, these planets' radii are consistent with theoretical mass–radius relationships and show no evidence of inflation. Neither would we expect radius inflation for these planets; radius inflation has only been observed for planets with $T_{\text{eq}} \gtrsim 1000$ K (e.g., Thorngren et al. 2016), and due to the low luminosities of M-dwarf host stars, all giant planets found so far around such stars have $T_{\text{eq}} \lesssim 1000$ K.

The two newly discovered planets, TOI 4201 b and TOI 5344 b, are both around high-metallicity host stars. TOI 4201 has a spectroscopically measured $[\text{Fe}/\text{H}] = 0.390 \pm 0.090$ and an a posteriori value of $[\text{Fe}/\text{H}] = 0.433 \pm 0.085$ based on the joint analysis, while TOI 5344 has a spectroscopic metallicity of $[\text{Fe}/\text{H}] = 0.390 \pm 0.090$ and an a posteriori value of $[\text{Fe}/\text{H}] = 0.425 \pm 0.088$. We also confirm high metallicities for the reanalyzed systems, with spectroscopic metallicities from HIRES of -0.010 ± 0.090 , 0.48 ± 0.09 , and 0.12 ± 0.09 for TOI 519, TOI 3629, and TOI 3714, respectively, and a posteriori values of 0.264 ± 0.083 , 0.549 ± 0.093 , and 0.390 ± 0.086 . As shown in Figure 8, other giant-planet-hosting M-dwarf stars also tend to have supersolar metallicities, and in fact there may be a trend toward higher metallicities for cooler short-period giant-planet-hosting stars. A strong correlation between host star metallicity and short-period giant planet occurrence has previously been established for FGK host stars (Fischer & Valenti 2005). The emerging set of giant-planet-hosting M dwarfs appears to show this trend as well (e.g., Hirano et al. 2018; Gan et al. 2022; Kagitani et al. 2023). The newly discovered systems bolster this conclusion. A caveat is that the metallicities that are shown in Figure 8 are taken directly from the NASA Exoplanet Archive and have been measured in an inhomogeneous fashion.

TOI-3629 $P=3.94d$ $M_p=0.24M_{Jup}$ $R_p=0.74R_{Jup}$ $M_S=0.63M_{Sun}$ $R_S=0.61R_{Sun}$

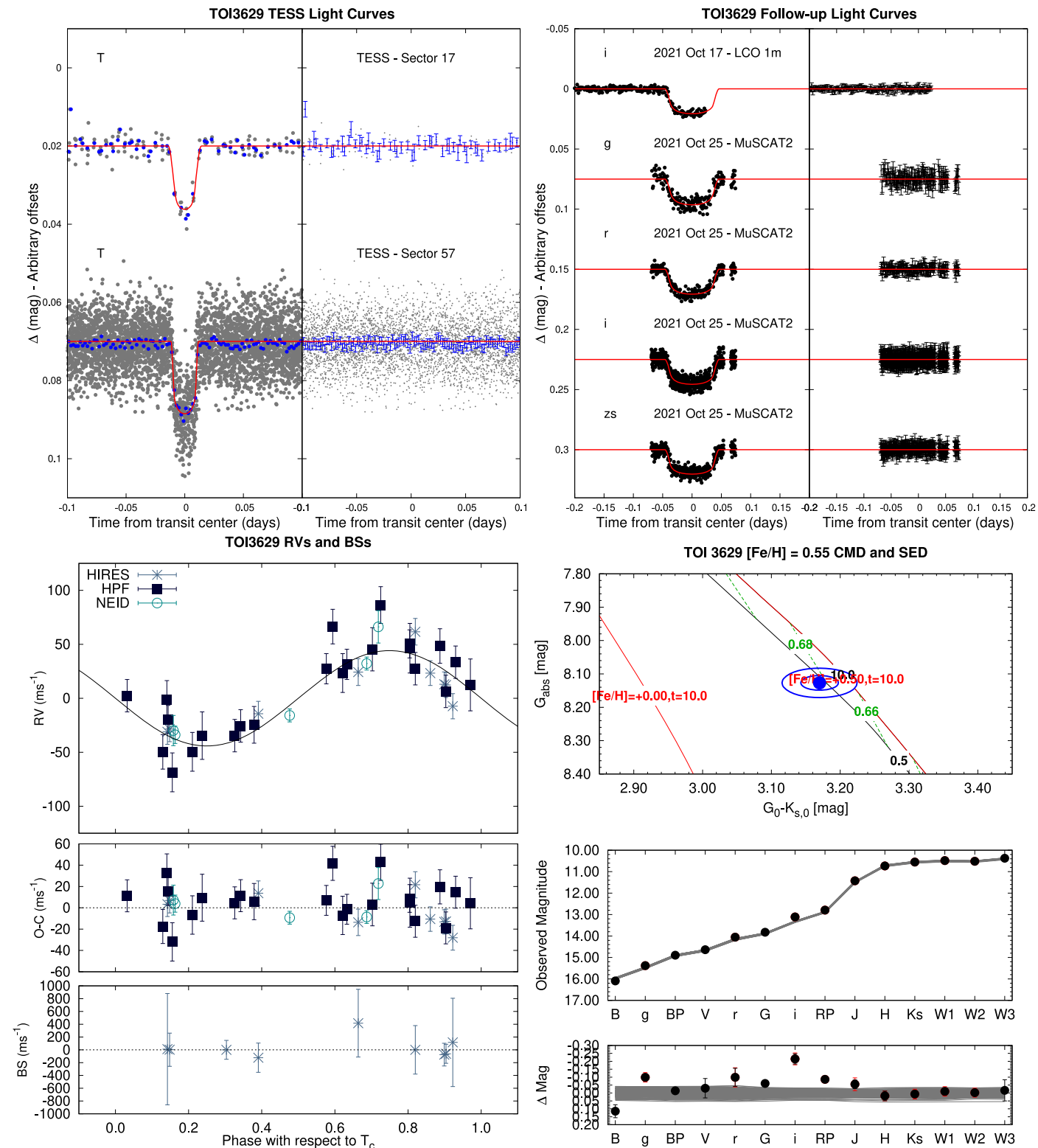


Figure 3. Same as Figure 1, but here we show the observations of TOI 3629 together with our best-fit model.

Moreover, the determination of M-dwarf metallicities from optical spectra may be subject to systematic errors. Indeed, the systematic differences between the metallicities measured from the optical spectra and the a posteriori metallicities for the five targets studied in this paper are typical for M dwarfs and

indicative of the difficulty of accurately measuring metallicities for M dwarfs based on either of these methods. An effort to homogeneously measure the metallicities of giant-planet-hosting M dwarfs using near-IR spectra might allow for a more robust conclusion.

TOI-3714 $P=2.15d$ $M_p=0.69M_{Jup}$ $R_p=0.99R_{Jup}$ $M_s=0.52M_{Sun}$ $R_s=0.50R_{Sun}$

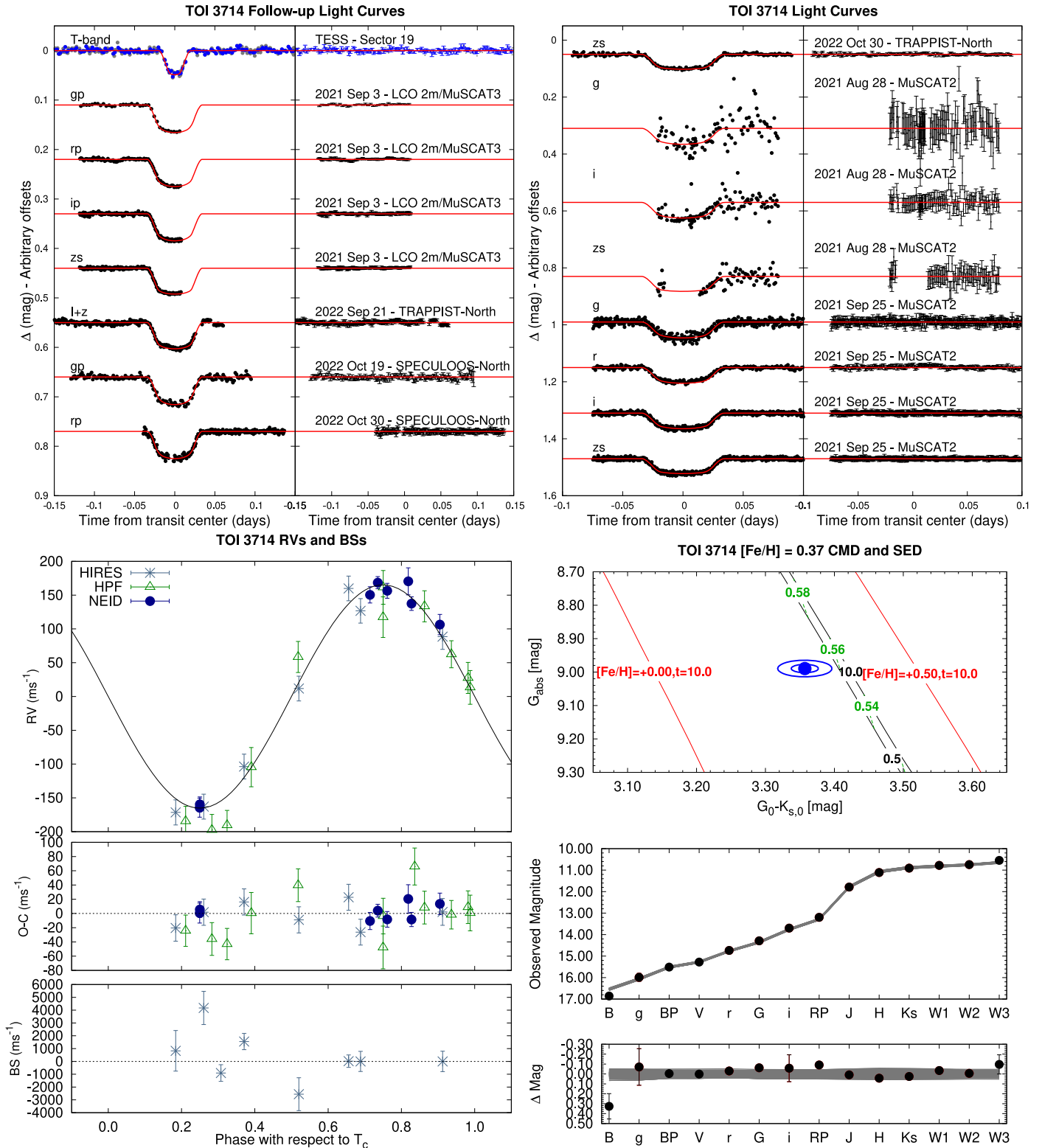


Figure 4. Same as Figure 1, but here we show the observations of TOI 3714 together with our best-fit model.

Table 10 compares the stellar and planetary masses and radii for TOI 519, TOI 3629, and TOI 3714 to the previously published values. We find that for TOI 3629 and TOI 3714 our values are within the error bars of the previous measurements. For both of these systems the planetary radius uncertainties are

reduced slightly, but the stellar mass uncertainties are larger owing to our method of treating systematic uncertainties. For TOI 519, our stellar mass estimate is approximately 2σ higher than that of Kagetani et al. (2023; when using our uncertainty; it is 4.6σ higher when using their uncertainty), but consistent

TOI-4201 $P=3.58d$ $M_p=2.57M_{Jup}$ $R_p=1.13R_{Jup}$ $M_s=0.63M_{Sun}$ $R_s=0.62R_{Sun}$

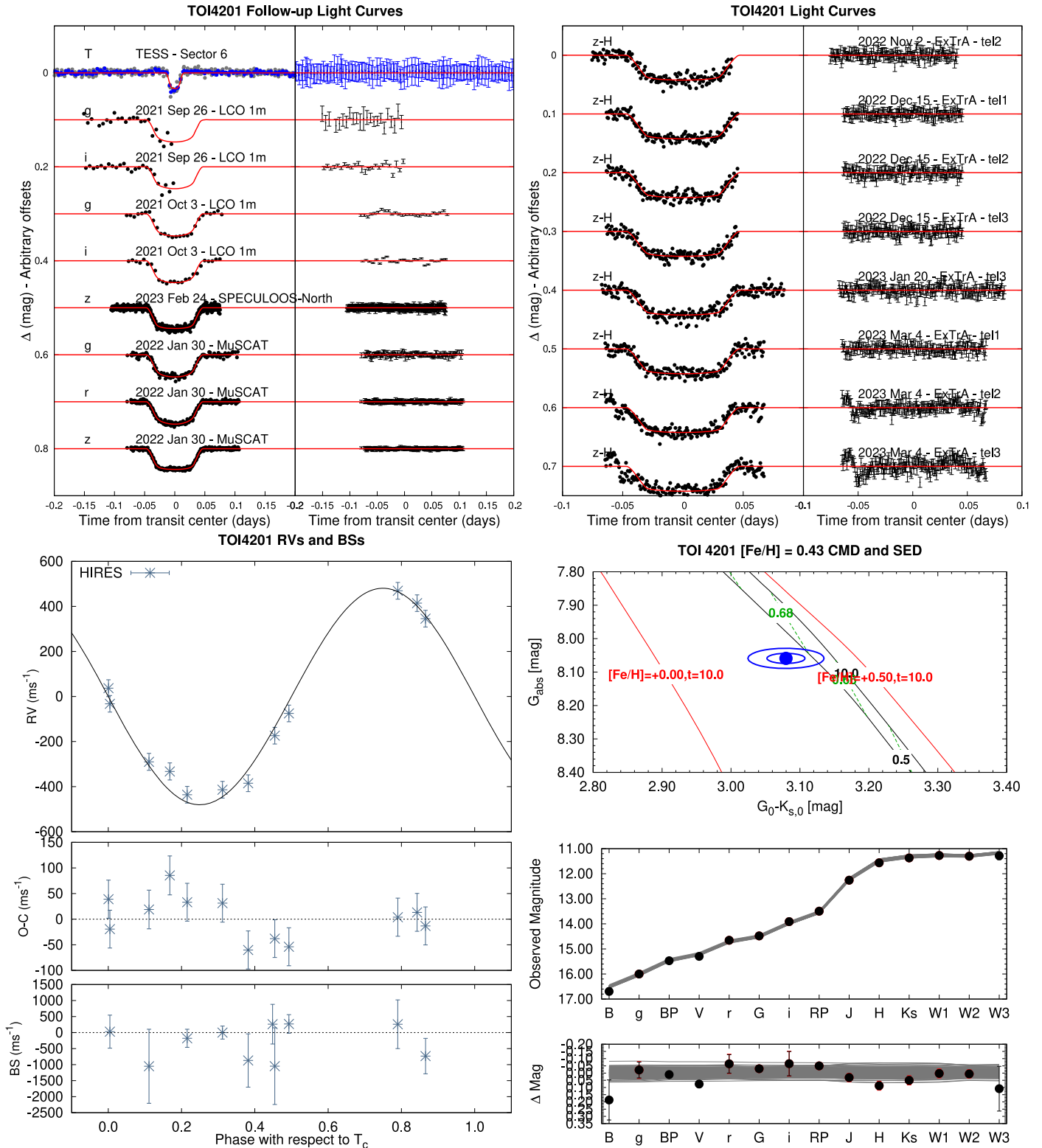


Figure 5. Same as Figure 1, but here we show the observations of TOI 4201 together with our best-fit model.

within the uncertainty of the value from Parviainen et al. (2021). The other values are consistent within the uncertainties, which are now somewhat smaller. We note that the stellar mass estimate from Kageyama et al. (2023) is close to the value of $0.3398 \pm 0.0086 M_{\odot}$ that comes from using the empirical

relation between stellar mass, absolute K_S magnitude, and metallicity determined by Mann et al. (2019).

The uncertainties on the parameters that we measure for all of the systems studied in this paper account for systematic uncertainties in the stellar evolution models, in a manner that

TOI-5344 $P=3.79d$ $M_p=0.41M_{Jup}$ $R_p=0.95R_{Jup}$ $M_S=0.61M_{Sun}$ $R_S=0.59R_{Sun}$

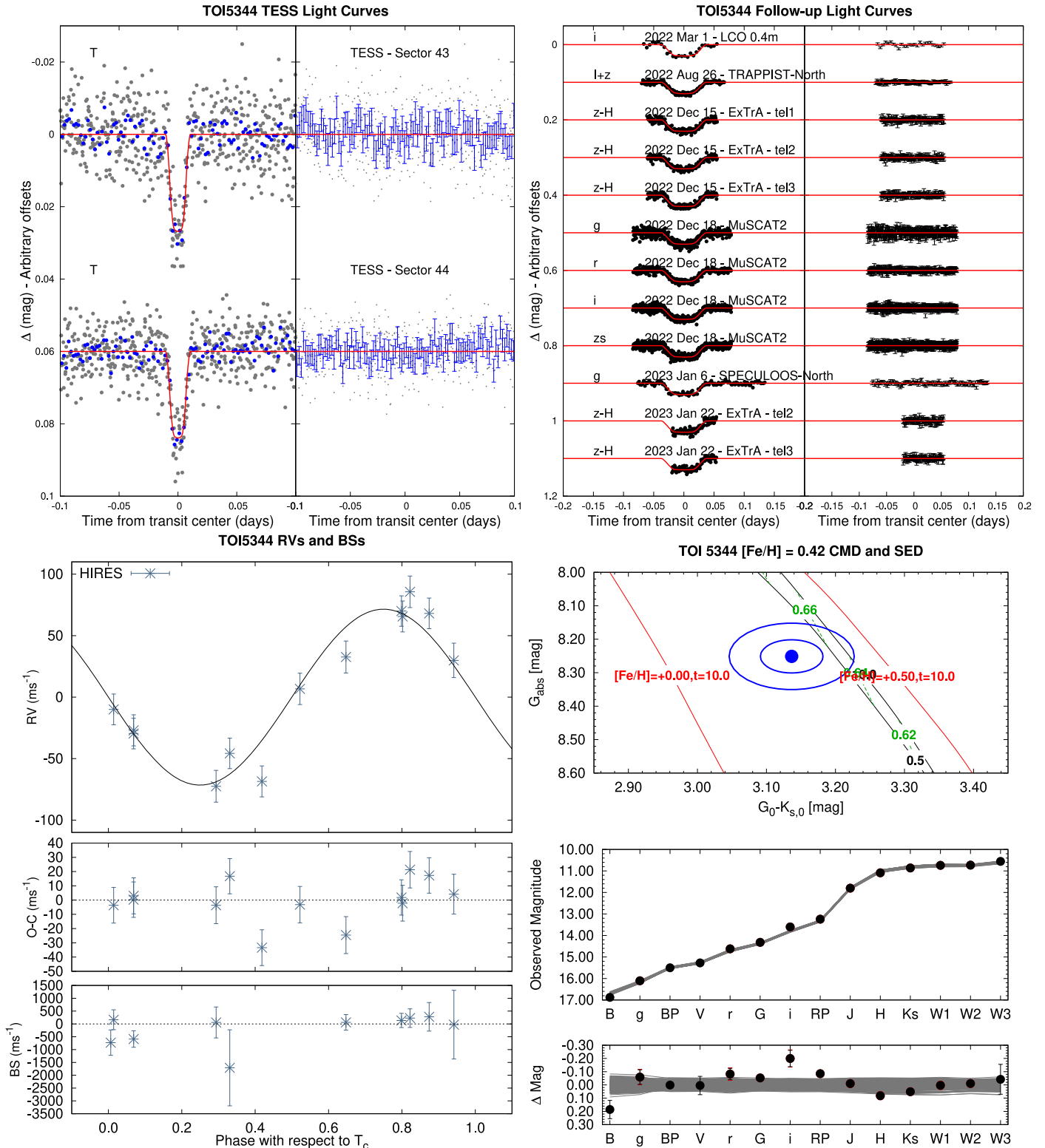


Figure 6. Same as Figure 1, but here we show the observations of TOI 5344 together with our best-fit model.

self-consistently allows for empirical constraints on the parameters that may reduce the uncertainties below the systematic errors. We measure stellar masses of $0.372 \pm 0.018 M_{\odot}$, $0.635 \pm 0.032 M_{\odot}$, $0.522 \pm 0.028 M_{\odot}$, $0.626 \pm$

$0.033 M_{\odot}$, and $0.612 \pm 0.034 M_{\odot}$, for TOI 519, TOI 3629, TOI 3714, TOI 4201, and TOI 5344, respectively. The relative uncertainties on the masses are thus 4.8%, 5.0%, 5.4%, 5.3%, and 5.6%, respectively, and comparable to the assumed 5%

Table 6

Adopted Derived Stellar Parameters for Newly Discovered Systems TOI 4201 and TOI 5344

Parameter	TOI 4201 Value	TOI 5344 Value
M_* (M_\odot)	0.626 ± 0.033	0.612 ± 0.034
R_* (R_\odot)	0.616 ± 0.012	0.588 ± 0.011
$\log g_*$ (cgs)	4.6553 ± 0.0100	4.686 ± 0.014
ρ_* (g cm^{-3})	3.775 ± 0.083	4.24 ± 0.14
L_* (L_\odot)	0.0809 ± 0.0062	0.0613 ± 0.0049
$T_{\text{eff}*}$ (K)	3926 ± 65	3747 ± 64
[Fe/H]	0.433 ± 0.085	0.425 ± 0.088
Age (Gyr)	$16.8^{+2.2}_{-4.9}$	10.9 ± 5.8
A_V (mag)	0.053 ± 0.017	0.536 ± 0.068
Distance (pc)	189.16 ± 0.65	136.88 ± 0.44

Note. The listed parameters are those determined through the joint differential evolution Markov chain analysis, including systematic errors in the stellar evolution models, described in Section 3.2. For all systems the RV observations are consistent with a circular orbit, and we assume a fixed circular orbit in generating the parameters listed here.

Table 7

Adopted Derived Stellar Parameters for Previously Discovered Systems TOI 519, TOI 3629, and TOI 3714

Parameter	TOI 519 Value	TOI 3629 Value	TOI 3714 Value
M_* (M_\odot)	0.372 ± 0.018	0.635 ± 0.032	0.522 ± 0.028
R_* (R_\odot)	0.3578 ± 0.0063	0.6103 ± 0.0099	$0.4958^{+0.0104}_{-0.0079}$
$\log g_*$ (cgs)	4.9016 ± 0.0085	4.670 ± 0.013	4.7638 ± 0.0097
ρ_* (g cm^{-3})	11.45 ± 0.18	$3.922^{+0.138}_{-0.096}$	6.01 ± 0.12
L_* (L_\odot)	0.0146 ± 0.0012	0.0750 ± 0.0068	0.0392 ± 0.0038
$T_{\text{eff}*}$ (K)	3354 ± 63	3865 ± 79	3652 ± 81
[Fe/H]	0.264 ± 0.083	0.549 ± 0.093	0.390 ± 0.086
Age (Gyr)	$0.55^{+0.75}_{-0.19}$	$9.8^{+6.6}_{-4.8}$	$12.5^{+4.9}_{-6.5}$
A_V (mag)	$0.0110^{+0.0100}_{-0.0070}$	0.163 ± 0.029	0.046 ± 0.015
Distance (pc)	114.88 ± 0.48	130.34 ± 0.30	113.12 ± 0.30

Note. The listed parameters are those determined through the joint differential evolution Markov chain analysis, including systematic errors in the stellar evolution models, described in Section 3.2. For all systems the RV observations are consistent with a circular orbit, and we assume a fixed circular orbit in generating the parameters listed here.

systematic uncertainty on the stellar masses. For comparison, we find typical uncertainties of $\sim 1\%$ – 2% when we do not account for systematic errors in the analysis.

We can also compare the stellar masses to the values predicted from the empirical relation between stellar mass, absolute K_S magnitude, and metallicity determined by Mann et al. (2019). Using this relation, we find masses of $0.3398 \pm 0.0086 M_\odot$, 0.604 ± 0.016 , $0.503 \pm 0.012 M_\odot$, $0.603 \pm 0.016 M_\odot$, and $0.574 \pm 0.015 M_\odot$ for TOI 519, TOI 3629, TOI 3714, TOI 4201, and TOI 5344, respectively. The masses from the empirical relations are systematically lower than the masses that we adopt based on the MIST isochrones. They are consistent with our values to within 1σ – 2σ . Our adopted uncertainties are also about twice as large as the uncertainty estimates based on the empirical relations.

The stellar effective temperatures that come from our modeling are more tightly constrained than the assumed systematic uncertainty. We measure respective a posteriori temperatures of 3354 ± 63 K, 3865 ± 79 K, 3652 ± 81 K, 3926 ± 65 K, and 3747 ± 64 K, with corresponding fractional

Table 8

Adopted Orbital and Planetary Parameters for Newly Discovered Planets TOI 4201 b and TOI 5344 b

Parameter	TOI 4201 b Value	TOI 5344 b Value
Light-curve parameters:		
P (days)	3.5819134 ± 0.0000017	3.7926220 ± 0.0000062
T_c (BJD_TDB) ^a	$2459864.32835 \pm 0.00011$	$2459848.99030 \pm 0.00019$
T_{14} (days) ^a	0.09294 ± 0.00042	0.07388 ± 0.00062
$T_{12} = T_{34}$ (days) ^a	0.01725 ± 0.00039	0.02077 ± 0.00072
a/R_*	13.70 ± 0.10	14.78 ± 0.16
ζ/R_* ^b	26.31 ± 0.18	36.10 ± 0.42
R_p/R_*	0.1886 ± 0.0014	0.1653 ± 0.0014
b^2	$0.165^{+0.017}_{-0.018}$	$0.540^{+0.014}_{-0.017}$
$b \equiv a \cos i/R_*$	$0.406^{+0.020}_{-0.023}$	$0.7348^{+0.0094}_{-0.0113}$
i (deg)	88.30 ± 0.10	87.150 ± 0.067
Limb-darkening coefficients ^c		
c_1, g	0.42 ± 0.11	0.22 ± 0.13
c_2, g	0.37 ± 0.15	0.14 ± 0.16
c_1, r	0.524 ± 0.090	0.25 ± 0.13
c_2, r	0.21 ± 0.14	0.29 ± 0.15
c_1, i	0.38 ± 0.14	0.22 ± 0.12
c_2, i	0.30 ± 0.17	0.13 ± 0.15
c_1, zS	0.125 ± 0.070	0.18 ± 0.12
c_2, zS	0.44 ± 0.13	0.21 ± 0.15
$c_1, I+z$...	0.31 ± 0.14
$c_2, I+z$...	0.33 ± 0.16
$c_1, z-H$	0.178 ± 0.089	0.18 ± 0.12
$c_2, z-H$	0.17 ± 0.14	0.02 ± 0.14
c_1, T	0.31 ± 0.16	0.21 ± 0.13
c_2, T	0.27 ± 0.18	0.17 ± 0.17
RV parameters:		
K (m s^{-1})	466 ± 21	74.4 ± 6.8
e^d	<0.083	<0.054
RV jitter HIRES ^e (m s^{-1})	43 ± 13	15.2 ± 4.6
Planetary parameters:		
M_p (M_J)	2.57 ± 0.15	0.412 ± 0.040
R_p (R_J)	1.130 ± 0.024	0.946 ± 0.021
$C(M_p, R_p)^f$	0.49	0.25
ρ_p (g cm^{-3})	2.21 ± 0.13	0.604 ± 0.063
$\log g_p$ (cgs)	3.699 ± 0.022	3.058 ± 0.042
a (au)	0.03924 ± 0.00069	0.04041 ± 0.00075
T_{eq} (K)	750 ± 13	689 ± 12
Θ^g	0.284 ± 0.014	0.0574 ± 0.0054
$\log_{10}(F)$ (cgs) ^h	7.855 ± 0.030	7.709 ± 0.031

Notes. For all systems we adopt a model in which the orbit is assumed to be circular. See the discussion in Section 3.2.

^a Times are in Barycentric Julian Date calculated on the Barycentric Dynamical Time (TDB) system. T_c : reference epoch of mid-transit that minimizes the correlation with the orbital period; T_{12} : total transit duration, time between first to last contact; $T_{12} = T_{34}$: ingress/egress time, time between first and second contact or between third and fourth contact.

^b Reciprocal of the half duration of the transit used as a jump parameter in our MCMC analysis in place of a/R_* . It is related to a/R_* by the expression $\zeta/R_* = a/R_*(2\pi(1 + e \sin \omega))/(P\sqrt{1 - b^2}\sqrt{1 - e^2})$ (Bakos et al. 2010).

^c Values for a quadratic law. The limb-darkening parameters were directly varied in the fit, using the tabulations from Claret et al. (2012, 2013) and Claret (2018) to place Gaussian prior constraints on their values, assuming a prior uncertainty of 0.2 for each coefficient.

^d The 95% confidence upper limit on the eccentricity determined when $\sqrt{e} \cos \omega$ and $\sqrt{e} \sin \omega$ are allowed to vary in the fit.

^e Term added in quadrature to the formal RV uncertainties for each instrument. This is treated as a free parameter in the fitting routine.

^f Correlation coefficient between the planetary mass M_p and radius R_p estimated from the posterior parameter distribution.

^g The Safronov number is given by $\Theta = \frac{1}{2}(V_{\text{esc}}/V_{\text{orb}})^2 = (a/R_p)(M_p/M_*)$ (see Hansen & Barman 2007).

^h Incoming flux per unit surface area, averaged over the orbit.

uncertainties of 1.9%, 2.0%, 2.2%, 1.7%, and 1.7%, whereas the assumed systematic uncertainty is 2.4%. This uncertainty is still much higher than the typical $\sim 0.2\%$ uncertainty that

Table 9
Adopted Orbital and Planetary Parameters for Previously Discovered Planets TOI 519 b, TOI 3629 b, and TOI 3714 b

Parameter	TOI 519 b Value	TOI 3629 b Value	TOI 3714 b Value
Light-curve parameters:			
P (days)	$1.26523248 \pm 0.00000012$	3.9365578 ± 0.0000043	$2.15484802 \pm 0.00000075$
T_c (BJD_TDB) ^a	$2459013.152990 \pm 0.000036$	$2459662.10795 \pm 0.00019$	$2459687.365240 \pm 0.000075$
T_{14} (days) ^a	0.05149 ± 0.00020	0.09139 ± 0.00050	0.06776 ± 0.00029
$T_{12} = T_{34}$ (days) ^a	0.01310 ± 0.00023	0.01119 ± 0.00030	0.01382 ± 0.00028
a/R_*	9.901 ± 0.053	$14.76^{+0.17}_{-0.12}$	11.391 ± 0.078
ζ/R_* ^b	51.77 ± 0.35	24.92 ± 0.17	36.85 ± 0.23
R_p/R_*	0.3040 ± 0.0021	0.1247 ± 0.0014	0.2057 ± 0.0013
b^2	$0.098^{+0.014}_{-0.014}$	$0.106^{+0.021}_{-0.021}$	$0.188^{+0.015}_{-0.016}$
$b \equiv a \cos i/R_*$	$0.313^{+0.022}_{-0.024} \& 0.325^{+0.030}_{-0.039}$	$0.433^{+0.017}_{-0.020}$	
i (deg)	88.19 ± 0.14	88.74 ± 0.14	87.830 ± 0.098
Limb-darkening coefficients: ^c			
c_1, B	0.24 ± 0.14
c_2, B	0.21 ± 0.18
c_1, g	0.51 ± 0.11	0.39 ± 0.12	0.55 ± 0.11
c_2, g	0.35 ± 0.16	0.35 ± 0.15	0.26 ± 0.16
c_1, r	0.53 ± 0.10	0.49 ± 0.12	0.55 ± 0.10
c_2, r	0.22 ± 0.15	0.14 ± 0.16	0.16 ± 0.15
c_1, i	0.404 ± 0.089	0.370 ± 0.093	0.389 ± 0.096
c_2, i	0.18 ± 0.14	0.26 ± 0.15	0.30 ± 0.15
c_1, z_s	0.329 ± 0.081	0.254 ± 0.096	0.288 ± 0.081
c_2, z_s	0.11 ± 0.14	0.26 ± 0.15	0.23 ± 0.13
$c_1, I+z$	0.38 ± 0.11
$c_2, I+z$	0.15 ± 0.16
$c_1, z-H$	0.141 ± 0.080
$c_2, z-H$	0.32 ± 0.13
c_1, T	0.233 ± 0.097	0.29 ± 0.11	0.18 ± 0.12
c_2, T	0.46 ± 0.15	0.22 ± 0.17	0.16 ± 0.16
RV parameters:			
K (m s ⁻¹)	191 ± 22	42.2 ± 3.2	167.1 ± 4.1
e^d	<0.048	<0.056	<0.047
RV jitter HIRES ^e (m s ⁻¹)	73 ± 28	15.2 ± 5.7	18.1 ± 6.7
RV jitter IRD ^e (m s ⁻¹)	23.8 ± 9.6
RV jitter HPF ^e (m s ⁻¹)	...	<7.2	<30.2
RV jitter NEID ^e (m s ⁻¹)	...	<7.2	<10.4
Planetary parameters:			
M_p (M_J)	0.525 ± 0.064	0.243 ± 0.020	0.689 ± 0.030
R_p (R_J)	1.059 ± 0.020	0.740 ± 0.014	0.994 ± 0.020
$C(M_p, R_p)^f$	0.23	0.28	0.69
ρ_p (g cm ⁻³)	0.551 ± 0.067	0.743 ± 0.064	0.871 ± 0.039
$\log g_p$ (cgs)	3.066 ± 0.053	3.042 ± 0.035	3.238 ± 0.015
a (au)	0.01648 ± 0.00027	0.04194 ± 0.00071	0.02630 ± 0.00046
T_{eq} (K)	754 ± 14	711 ± 15	764 ± 17
Θ^g	0.0439 ± 0.0052	0.0432 ± 0.0033	0.0694 ± 0.0023
$\log_{10}\langle F \rangle$ (cgs) ^h	7.865 ± 0.033	7.763 ± 0.036	7.888 ± 0.040

Notes. For all systems we adopt a model in which the orbit is assumed to be circular. See the discussion in Section 3.2.

^a Times are in Barycentric Julian Date calculated on the Barycentric Dynamical Time (TDB) system. T_c : reference epoch of mid-transit that minimizes the correlation with the orbital period; T_{12} : total transit duration, time between first to last contact; $T_{12} = T_{34}$: ingress/egress time, time between first and second contact or between third and fourth contact.

^b Reciprocal of the half duration of the transit used as a jump parameter in our MCMC analysis in place of a/R_* . It is related to a/R_* by the expression $\zeta/R_* = a/R_*(2\pi(1 + e \sin \omega))/(P\sqrt{1 - b^2}\sqrt{1 - e^2})$ (Bakos et al. 2010).

^c Values for a quadratic law. The limb-darkening parameters were directly varied in the fit, using the tabulations from Claret et al. (2012, 2013) and Claret (2018) to place Gaussian prior constraints on their values, assuming a prior uncertainty of 0.2 for each coefficient.

^d The 95% confidence upper limit on the eccentricity determined when $\sqrt{e} \cos \omega$ and $\sqrt{e} \sin \omega$ are allowed to vary in the fit.

^e Term added in quadrature to the formal RV uncertainties for each instrument. This is treated as a free parameter in the fitting routine.

^f Correlation coefficient between the planetary mass M_p and radius R_p estimated from the posterior parameter distribution.

^g The Safronov number is given by $\Theta = \frac{1}{2}(V_{\text{esc}}/V_{\text{orb}})^2 = (a/R_p)(M_p/M_*)$ (see Hansen & Barman 2007).

^h Incoming flux per unit surface area, averaged over the orbit.

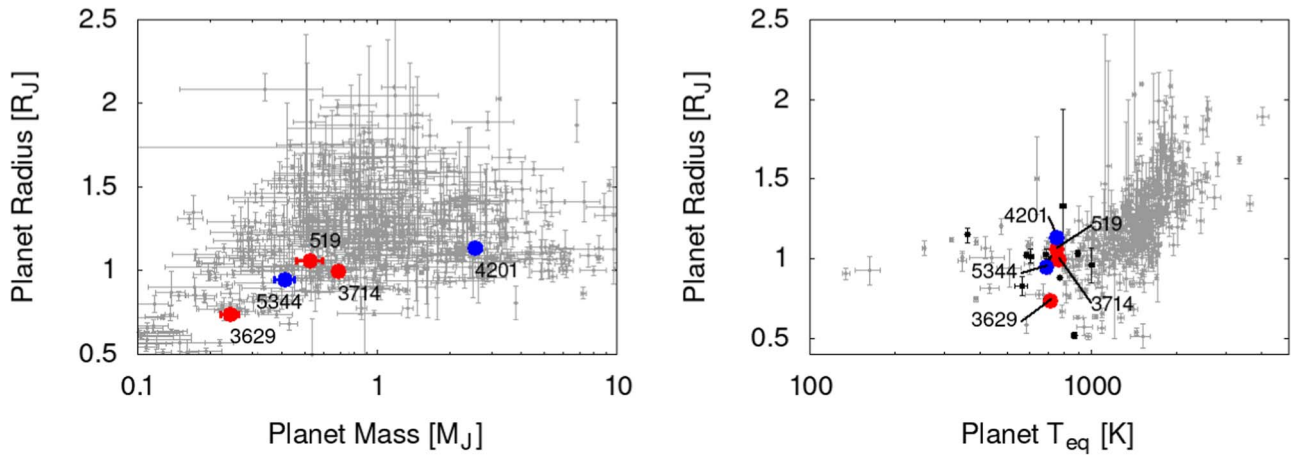


Figure 7. Left: planet radius vs. mass. The two new planet discoveries and the three other systems that we reanalyze are indicated. Small gray points show all transiting giant planets with $M_p > 0.1 M_J$ and $R_p > 0.5 R_J$ from the NASA Exoplanet Archive. Right: planet radius vs. equilibrium temperature for transiting giant planets. The equilibrium temperature is estimated assuming zero albedo and full redistribution of heat, so that it is effectively a proxy for the flux received from the star. The small black points show planets that orbit M dwarfs ($T_{\text{eff}\star} < 4000$ K), while the gray points show all other planets. None of the transiting giant planets discovered around M dwarfs to date appear to be inflated, but all have low equilibrium temperatures where planet inflation has not been observed for hotter host stars either.

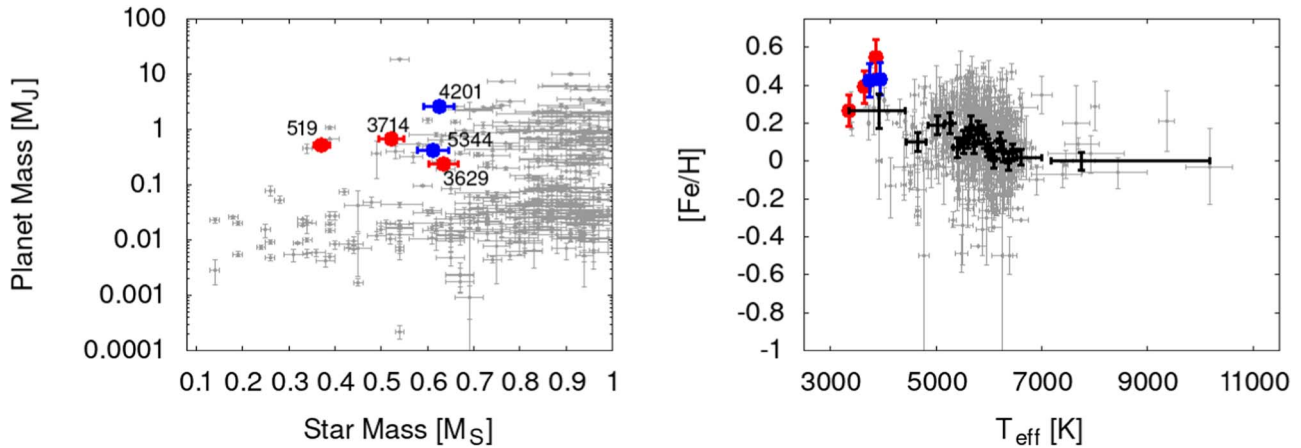


Figure 8. Left: planet mass vs. host star mass. The two new planet discoveries and the three other systems that we reanalyze are indicated. Small gray points show all transiting planets with host star masses less than $1 M_\odot$ from the NASA Exoplanet Archive. Right: metallicity vs. effective temperature for the host stars of transiting short-period giant planets with $P < 10$ days, $R_p > 0.5 R_J$, and $M_p > 0.1 M_J$ (small gray points). The host stars of the five systems analyzed in this paper are indicated with the same colors as in the left panel. The black points show the median $[\text{Fe}/\text{H}]$ vs. T_{eff} when binning the sample into bins of 25 stars. The vertical error bars show the standard deviation within the bin, while the horizontal error bars show the width of the bin. We confirm high metallicities for the three reanalyzed systems and find that the two newly discovered systems also have high metallicities. This supports earlier findings that giant-planet-hosting M dwarfs have high metallicity and that the metallicity–giant planet occurrence relation may be even stronger for M dwarfs than for hotter host stars.

Table 10
Comparison to Literature Parameters for TOI 519, TOI 3629, and TOI 3714

Parameter	TOI 519	TOI 519	TOI 519	TOI 3629	TOI 3629	TOI 3714	TOI 3714
	This Paper	(Kagetani et al. 2023)	(Parviainen et al. 2021)	This Paper	(Cañas et al. 2022)	This Paper	(Cañas et al. 2022)
$M_\star (M_\odot)$	0.372 ± 0.018	0.335 ± 0.008	$0.369^{+0.026}_{-0.097}$	0.635 ± 0.032	0.63 ± 0.02	0.522 ± 0.028	0.53 ± 0.02
$R_\star (R_\odot)$	0.3578 ± 0.0063	0.350 ± 0.010	$0.373^{+0.020}_{-0.088}$	0.6103 ± 0.0099	$0.60^{+0.02}_{-0.01}$	$0.4958^{+0.0104}_{-0.0079}$	
$M_p (M_J)$	0.525 ± 0.064	$0.463^{+0.082}_{-0.088}$...	0.243 ± 0.020	0.26 ± 0.02	0.51 ± 0.01	0.689 ± 0.030
$R_p (R_J)$	1.059 ± 0.020	1.03 ± 0.03	1.06 ± 0.17	0.740 ± 0.014	0.74 ± 0.02	0.994 ± 0.020	1.01 ± 0.03

results when systematic errors are not accounted for in the modeling. The constraints on ρ_\star from the transit observations, together with constraints on the luminosity from the observed magnitudes and parallaxes, allow the effective temperature to be more tightly constrained than the assumed systematic error on this parameter in the stellar evolutionary models.

The systematic errors feed into most of the other parameters as well. The median stellar radius and planetary radius fractional uncertainties are 1.9% and 2.0%, respectively, whereas we typically find $\sim 0.5\%$ and 1.0% respective uncertainties when not including systematic errors. For comparison, Tayar et al. (2022) suggest a systematic stellar

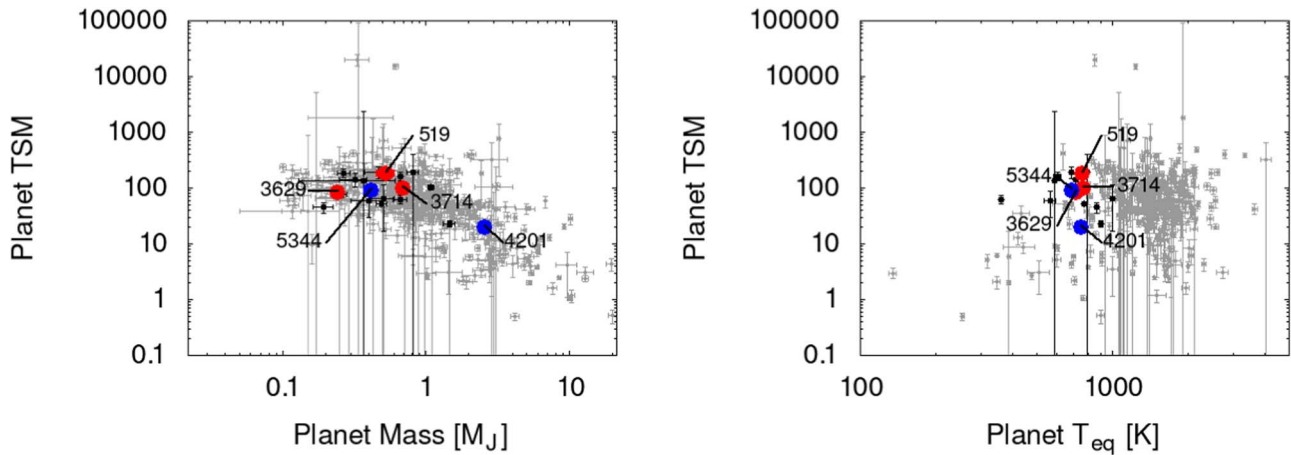


Figure 9. Left: TSM vs. planet mass. The two new planet discoveries and the three other systems that we reanalyze are indicated. Small gray points show all transiting planets with measured masses $>0.1 M_J$ and radii $>0.5 R_J$ from the NASA Exoplanet Archive, while small black points highlight those planets that orbit M-dwarf stars. Right: TSM vs. planet T_{eq} computed assuming zero albedo and full redistribution of heat. The symbols are the same as in the left panel. TOI 519 b is the most favorable of the planets discussed in this paper for transmission spectroscopy. In general, giant planets transiting M dwarfs are among the highest TSM systems with $T_{\text{eq}} < 1000$ K.

radius uncertainty of 4.2%, which would set a comparable uncertainty on the planetary radius; however, this uncertainty does not account for other empirical constraints that can reduce the uncertainty below this limit, as we do here. We find that the planetary mass uncertainties are largely set by the uncertainty on the RV semiamplitude K , which exceeds the stellar mass uncertainty for most of the systems. The only exception is TOI 3714 b, for which the fractional uncertainty on K is 2.5%, so that the planetary mass fractional uncertainty of 4.4% is largely set by the stellar mass uncertainty. The planetary surface gravity $\log g_p$ is a special case. This parameter is determined from a combination of directly measured parameters (K , R_p/R_* , a/R_* , i , and P ; Southworth et al. 2007) that are largely independent of the stellar parameters. In the case of the systems studied here, the uncertainties on K are the main contributors to the uncertainties on the planetary surface gravities, and these uncertainties are not significantly affected by our method of treating systematic errors in the stellar evolution models.

Due to the small radii of the host stars, giant planets transiting M dwarfs are among the most favorable targets for performing transmission spectroscopy on low equilibrium temperature giant planets. Figure 9 compares the transmission spectroscopy metric (TSM; Kempton et al. 2018) of the five systems discussed in this paper to that of other transiting giant planets from the NASA Exoplanet Archive. When compared against other planets of comparable mass, giant planets around M dwarfs do not have particularly high values of TSM. This is because the relatively small scale heights of these cool, uninflated planets lead to lower TSM values compared to highly inflated hot Jupiters. However, when comparing against other planets with $T_{\text{eq}} \lesssim 1000$ K, giant planets around M dwarfs tend to have relatively high values of TSM. Among the targets discussed in this paper, TOI 519 b is the most favorable target for transmission spectroscopy, with $\text{TSM} = 186 \pm 28$, while the more massive planet TOI 4201 b is relatively unfavorable, with $\text{TSM} = 20 \pm 2$.

Acknowledgments

The authors thank the anonymous referee for helpful comments that have improved the quality of the paper. J.H., G.B., and Z.C. acknowledge funding from NASA grant

80NSSC22K0315. This work is based in part on observations made with the Keck I telescope at Maunakea Observatory, Hawaii. Time on this facility was awarded through NASA. We would like to acknowledge the following individuals who contributed to gathering the Keck I/HIRES observations presented in this paper: I. Angelo, A. Polanski, S. Yee, D. Tyler, C. Beard, J. Van Zandt, J. Akana Murphy, A. Mayo, E. Petigura, L. Weiss, G. Gilbert, L. Handley, M. MacDougall, F. Dai, A. Householder, M. Rice, N. Saunders, J. Zhang, C. Brinkman, M. He, A. Langford, D. Pidhorodetska, J. Lubin, S. Blunt, E. Turtelboom, E. Loudon, S. Dulz, and D. Shaw. The authors wish to recognize and acknowledge the very significant cultural role and reverence that the summit of Maunakea has always had within the indigenous Hawaiian community. We are most fortunate to have the opportunity to conduct observations from this mountain. We acknowledge T. Gan for contributing to the data reduction of observations from the LCOGT facilities. This work is partly supported by JSPS KAKENHI grant Nos. JP17H04574, JP18H05439, and JP21K20376 and JST CREST grant No. JPMJCR1761. E.P. acknowledges funding from the Spanish Ministry of Economics and Competitiveness through project PID2021-125627OB-C32. E.E-B. acknowledges financial support from the European Union and the State Agency of Investigation of the Spanish Ministry of Science and Innovation (MICINN) under the grant PRE2020-093107 of the Pre-Doc Program for the Training of Doctors (FPI-SO) through FSE funds. This article is based on observations made with the MuSCAT2 instrument, developed by ABC, at Telescopio Carlos Sánchez operated on the island of Tenerife by the IAC in the Spanish Observatorio del Teide. This paper is based on observations made with the MuSCAT3 instrument, developed by the Astrobiology Center and under financial supports by JSPS KAKENHI (JP18H05439) and JST PRESTO (JPMJPR1775), at Faulkes Telescope North on Maui, Hawaii, operated by the Las Cumbres Observatory. A.J. acknowledges support from ANID—Millennium Science Initiative—ICN12_009 and from FONDECYT project 1210718. R.B. acknowledges support from ANID—Millennium Science Initiative—ICN12_009 and from FONDECYT project 11200751. H.P. acknowledges support from the Spanish Ministry of Science and Innovation with the Ramon

y Cajal fellowship No. RYC2021-031798-I. Funding from the University of La Laguna and the Spanish Ministry of Universities is acknowledged. Based on data collected under the ExTrA project at the ESO La Silla Paranal Observatory. ExTrA is a project of Institut de Planétologie et d’Astrophysique de Grenoble (IPAG/CNRS/UGA), funded by the European Research Council under the ERC grant agreement No. 337591-ExTrA. ExTrA has been supported by Labex OSUG@2020 (Investissements d’avenir—ANR10 LABX56), the “Programme National de Physique Stellaire” (PNPS), and the “Programme National de Planétologie of CNRS/INSU, cofunded by CEA and CNES. We thank the Swiss National Science Foundation (SNSF) and Geneva University for their continuous support to our planet search programs. This work has in particular been carried out in the frame of the National Centre for Competence in Research “Planets” supported by the Swiss National Science Foundation (SNSF). This research has made use of the NASA Exoplanet Archive, which is operated by the California Institute of Technology, under contract with the National Aeronautics and Space Administration under the Exoplanet Exploration Program. M.G. and A.T. acknowledge the support of the M.V. Lomonosov Moscow State University Program of Development. This work makes use of observations from the LCOGT network. Part of the LCOGT telescope time was granted by NOIRLab through the Mid-Scale Innovations Program (MSIP). MSIP is funded by NSF. This research has made use of the Exoplanet Follow-up Observation Program (ExoFOP; DOI: 10.26134/ExoFOP5) website, which is operated by the California Institute of Technology, under contract with the National Aeronautics and Space Administration under the Exoplanet Exploration Program. Funding for the TESS mission is provided by NASA’s Science Mission Directorate. K.A.C. acknowledges support from the TESS mission via subaward s3449 from MIT. This publication makes use of data products from the TRAPPIST project. TRAPPIST is funded by the Belgian National Fund for Scientific Research (F.R.S.-FNRS) under grant PDRT.0120.21. TRAPPIST-North is a project funded by the University of Liege (Belgium), in collaboration with Cadi Ayyad University of Marrakech (Morocco). E.J. is F.R.S.-FNRS Senior Research Associate. M.G. is F.R.S.-FNRS Research Director. The postdoctoral fellowship of K.B. is funded by F.R.S.-FNRS grant T.0109.20 and by the Franqui Foundation. The ULiege’s contribution to SPECULOOS has received funding from the European Research Council under the European Union’s Seventh Framework Programme (FP/2007-2013; grant agreement No. 336480/SPECULOOS), from the Balzan Prize and Franqui Foundations, from the Belgian Scientific Research Foundation (F.R.S.-FNRS; grant No. T.0109.20), from the University of Liege, and from the ARC grant for Concerted Research Actions financed by the Wallonia-Brussels Federation. SPECULOOS-North has received financial support from the Heising-Simons Foundation and from Dr. and Mrs. Colin Masson and Dr. Peter A. Gilman. This research received funding from the European Research Council (ERC) under the European Union’s Horizon 2020 research and innovation program (grant agreement No. 803193/BEBOP) and from the Science and Technology Facilities Council (STFC; grant No. ST/S00193X/1). This publication benefits from the support of the French Community of Belgium in the context of the FRIA Doctoral Grant awarded to M.T. We acknowledge the use of public TESS data from pipelines at the TESS Science Office and at the TESS Science


Processing Operations Center. Resources supporting this work were provided by the NASA High-End Computing (HEC) program through the NASA Advanced Supercomputing (NAS) Division at Ames Research Center for the production of the SPOC data products. This paper made use of data collected by the TESS mission, which are publicly available from the Mikulski Archive for Space Telescopes (MAST) operated by the Space Telescope Science Institute (STScI). Funding for the TESS mission is provided by NASA’s Science Mission Directorate. The specific observations from MAST analyzed in this paper can be accessed from DOI:10.17909/1cab-7p42.

Facilities: TESS, Keck:I, LCOGT, Sanchez, FTN, TRAPPIST, Subaru, HET, WIYN, Gaia, Exoplanet Archive.

Software: VARTOOLS (Hartman & Bakos 2016), MWDUST (Bovy et al. 2016), Astropy (Astropy Collaboration et al. 2013, 2018, 2022), AstroImageJ (Collins et al. 2017), TAPIR (Jensen 2013).

ORCID iDs

J. D. Hartman  <https://orcid.org/0000-0001-8732-6166>
 G. Á. Bakos  <https://orcid.org/0000-0001-7204-6727>
 A. W. Howard  <https://orcid.org/0000-0001-8638-0320>
 H. Isaacson  <https://orcid.org/0000-0002-0531-1073>
 S. Giacalone  <https://orcid.org/0000-0002-8965-3969>
 A. Chontos  <https://orcid.org/0000-0003-1125-2564>
 N. Narita  <https://orcid.org/0000-0001-8511-2981>
 A. Fukui  <https://orcid.org/0000-0002-4909-5763>
 J. P. de Leon  <https://orcid.org/0000-0002-6424-3410>
 N. Watanabe  <https://orcid.org/0000-0002-7522-8195>
 M. Mori  <https://orcid.org/0000-0002-5609-4427>
 T. Kagetani  <https://orcid.org/0000-0002-5331-6637>
 I. Fukuda  <https://orcid.org/0000-0002-9436-2891>
 Y. Kawai  <https://orcid.org/0000-0002-0488-6297>
 M. Ikoma  <https://orcid.org/0000-0002-5658-5971>
 E. Pallé  <https://orcid.org/0000-0003-0987-1593>
 F. Murgas  <https://orcid.org/0000-0001-9087-1245>
 E. Esparza-Borges  <https://orcid.org/0000-0002-2341-3233>
 H. Parviainen  <https://orcid.org/0000-0001-5519-1391>
 L. G. Bouma  <https://orcid.org/0000-0002-0514-5538>
 X. Bonfils  <https://orcid.org/0000-0001-9003-8894>
 J. M. Almenara  <https://orcid.org/0000-0003-3208-9815>
 Karen A. Collins  <https://orcid.org/0000-0001-6588-9574>
 Kevin I. Collins  <https://orcid.org/0000-0003-2781-3207>
 Howard M. Relles  <https://orcid.org/0009-0009-5132-9520>
 Khalid Barkaoui  <https://orcid.org/0000-0003-1464-9276>
 Richard P. Schwarz  <https://orcid.org/0000-0001-8227-1020>
 Ghachoui Mourad  <https://orcid.org/0000-0003-3986-0297>
 Artem Burdanov  <https://orcid.org/0000-0001-9892-2406>
 Julien de Wit  <https://orcid.org/0000-0003-2415-2191>
 Emmanuël Jehin  <https://orcid.org/0000-0001-8923-488X>
 Amaury H. M. J. Triaud  <https://orcid.org/0000-0002-5510-8751>
 Michaël Gillon  <https://orcid.org/0000-0003-1462-7739>
 Zouhair Benkhaldoun  <https://orcid.org/0000-0001-6285-9847>
 Keith Horne  <https://orcid.org/0000-0003-1728-0304>
 Ramotholo Sefako  <https://orcid.org/0000-0003-3904-6754>
 A. Jordán  <https://orcid.org/0000-0002-5389-3944>
 R. Brahm  <https://orcid.org/0000-0002-9158-7315>
 V. Suc  <https://orcid.org/0000-0001-7070-3842>
 Steve B. Howell  <https://orcid.org/0000-0002-2532-2853>
 E. Furlan  <https://orcid.org/0000-0001-9800-6248>

J. E. Schlieder  <https://orcid.org/0000-0001-5347-7062>
 D. Ciardi  <https://orcid.org/0000-0002-5741-3047>
 T. Barclay  <https://orcid.org/0000-0001-7139-2724>
 E. J. Gonzales  <https://orcid.org/0000-0002-9329-2190>
 I. Crossfield  <https://orcid.org/0000-0002-1835-1891>
 C. D. Dressing  <https://orcid.org/0000-0001-8189-0233>
 M. Goliguzova  <https://orcid.org/0000-0003-2228-7914>
 A. Tatarnikov  <https://orcid.org/0000-0002-4398-6258>
 George R. Ricker  <https://orcid.org/0000-0003-2058-6662>
 Roland Vanderspek  <https://orcid.org/0000-0001-6763-6562>
 David W. Latham  <https://orcid.org/0000-0001-9911-7388>
 S. Seager  <https://orcid.org/0000-0002-6892-6948>
 Joshua N. Winn  <https://orcid.org/0000-0002-4265-047X>
 Jon M. Jenkins  <https://orcid.org/0000-0002-4715-9460>
 Stephanie Striegel  <https://orcid.org/0009-0008-5145-0446>
 Avi Shporer  <https://orcid.org/0000-0002-1836-3120>
 Andrew Vanderburg  <https://orcid.org/0000-0001-7246-5438>
 Alan M. Levine  <https://orcid.org/0000-0001-8172-0453>
 Veselin B. Kostov  <https://orcid.org/0000-0001-9786-1031>
 David Watanabe  <https://orcid.org/0000-0002-3555-8464>

References

- Artigau, É., Hébrard, G., Cadieux, C., et al. 2021, *AJ*, 162, 144
 Artigau, É., Kouach, D., Donati, J.-F., et al. 2014, *Proc. SPIE*, 9147, 914715
 Astropy Collaboration, Price-Whelan, A. M., Lim, P. L., et al. 2022, *ApJ*, 935, 167
 Astropy Collaboration, Price-Whelan, A. M., Sipőcz, B. M., et al. 2018, *AJ*, 156, 123
 Astropy Collaboration, Robitaille, T. P., Tollerud, E. J., et al. 2013, *A&A*, 558, A33
 Barkaoui, K., Burdanov, A., Hellier, C., et al. 2019, *AJ*, 157, 43
 Bakos, G. Á., Bayliss, D., Bento, J., et al. 2018, arXiv:1812.09406
 Bakos, G. Á., Bayliss, D., Bento, J., et al. 2020, *AJ*, 159, 267
 Bakos, G. Á., Torres, G., Pál, A., et al. 2010, *ApJ*, 710, 1724
 Bayliss, D., Gillen, E., Eigmüller, P., et al. 2018, *MNRAS*, 475, 4467
 Bonfils, X., Almenara, J. M., Jocou, L., et al. 2015, *Proc. SPIE*, 9605, 96051L
 Bouma, L. G., Hartman, J. D., Bhatti, W., Winn, J. N., & Bakos, G. Á. 2019, *ApJS*, 245, 13
 Bovy, J., Rix, H.-W., Green, G. M., Schlafly, E. F., & Finkbeiner, D. P. 2016, *ApJ*, 818, 130
 Brown, T. M., Baliber, N., Bianco, F. B., et al. 2013, *PASP*, 125, 1031
 Bryant, E. M., Bayliss, D., & Van Eylen, V. 2023, *MNRAS*, 521, 3663
 Burdanov, A. Y., de Wit, J., Gillon, M., et al. 2022, *PASP*, 134, 105001
 Burn, R., Schlecker, M., Mordasini, C., et al. 2021, *A&A*, 656, A72
 Cañas, C. I., Kanodia, S., Bender, C. F., et al. 2022, *AJ*, 164, 50
 Cañas, C. I., Stefansson, G., Kanodia, S., et al. 2020, *AJ*, 160, 147
 Charbonneau, D., Brown, T. M., Noyes, R. W., & Gilliland, R. L. 2002, *ApJ*, 568, 377
 Choi, J., Dotter, A., Conroy, C., et al. 2016, *ApJ*, 823, 102
 Claret, A. 2018, *A&A*, 618, A20
 Claret, A., Hauschildt, P. H., & Witte, S. 2012, *A&A*, 546, A14
 Claret, A., Hauschildt, P. H., & Witte, S. 2013, *A&A*, 552, A16
 Clark, C. A., van Belle, G. T., Ciardi, D. R., et al. 2022, *AJ*, 163, 232
 Cointepas, M., Almenara, J. M., Bonfils, X., et al. 2021, *A&A*, 650, A145
 Collins, K. A., Kielkopf, J. F., Stassun, K. G., & Hessman, F. V. 2017, *AJ*, 153, 77
 Cutri, R. M., Wright, E. L., Conrow, T., et al. 2021, *yCat*, II/328
 Delrez, L., Gillon, M., Queloz, D., et al. 2018, *Proc. SPIE*, 10700, 107001I
 Dotter, A. 2016, *ApJS*, 222, 8
 Dressing, C. D., & Charbonneau, D. 2015, *ApJ*, 807, 45
 Eastman, J. D., Diamond-Lowe, H., & Tayar, J. 2023, *AJ*, 166, 132
 Fischer, D. A., & Valenti, J. 2005, *ApJ*, 622, 1102
 Fukui, A., Narita, N., Tristram, P. J., et al. 2011, *PASJ*, 63, 287
 Gaia Collaboration, Vallenari, A., Brown, A. G. A., et al. 2023, *A&A*, 674, A1
 Gan, T., Lin, Z., Wang, S. X., et al. 2022, *MNRAS*, 511, 83
 Gan, T., Wang, S. X., Wang, S., et al. 2023, *AJ*, 165, 17
 García, L. J., Timmermans, M., Pozuelos, F. J., et al. 2021, prose: FITS images processing pipeline, Astrophysics Source Code Library, ascl:2111.006
 García, L. J., Timmermans, M., Pozuelos, F. J., et al. 2022, *MNRAS*, 509, 4817
 Gillon, M., Jehin, E., Magain, P., et al. 2011, *EPJ Web Conf.*, 11, 06002
 Guerrero, N. M., Seager, S., Huang, C. X., et al. 2021, *ApJS*, 254, 39
 Halverson, S., Terrien, R., Mahadevan, S., et al. 2016, *Proc. SPIE*, 9908, 99086P
 Hansen, B. M. S., & Barman, T. 2007, *ApJ*, 671, 861
 Hartman, J. D., & Bakos, G. Á. 2016, *A&C*, 17, 1
 Hartman, J. D., Bakos, G. Á., Bayliss, D., et al. 2019, *AJ*, 157, 55
 Hartman, J. D., Bayliss, D., Brahm, R., et al. 2015, *AJ*, 149, 166
 Henry, T. J., Jao, W.-C., Winters, J. G., et al. 2018, *AJ*, 155, 265
 Hirano, T., Dai, F., Gandolfi, D., et al. 2018, *AJ*, 155, 127
 Hobson, M. J., Jordán, A., Bryant, E. M., et al. 2023, *ApJL*, 946, L4
 Houdebine, É. R., Mullan, D. J., Doyle, J. G., et al. 2019, *AJ*, 158, 56
 Howard, A. W., & Fulton, B. J. 2016, *PASP*, 128, 114401
 Howard, A. W., Johnson, J. A., Marcy, G. W., et al. 2010, *ApJ*, 721, 1467
 Howell, S. B., Everett, M. E., Sherry, W., Horch, E., & Ciardi, D. R. 2011, *AJ*, 142, 19
 Huang, C. X., Vanderburg, A., Pál, A., et al. 2020, *RNAAS*, 4, 204
 Jehin, E., Gillon, M., Queloz, D., et al. 2011, *Msngr*, 145, 2
 Jenkins, J. M., Caldwell, D. A., Chandrasekaran, H., et al. 2010, *ApJL*, 713, L87
 Jenkins, J. M., Twicken, J. D., McCauliff, S., et al. 2016, *Proc. SPIE*, 9913, 99133E
 Jensen, E. 2013, Tapir: a web interface for transit/eclipse observability, Astrophysics Source Code Library, ascl:1306.007
 Johnson, J. A., Aller, K. M., Howard, A. W., & Crepp, J. R. 2010, *PASP*, 122, 905
 Johnson, J. A., Gazak, J. Z., Apps, K., et al. 2012, *AJ*, 143, 111
 Jordán, A., Brahm, R., Espinoza, N., et al. 2019, *AJ*, 157, 100
 Jordán, A., Hartman, J. D., Bayliss, D., et al. 2022, *AJ*, 163, 125
 Kagetani, T., Narita, N., Kimura, T., et al. 2023, *PASJ*, 75, 713
 Kanodia, S., Libby-Roberts, J., Cañas, C. I., et al. 2022, *AJ*, 164, 81
 Kanodia, S., Mahadevan, S., Libby-Roberts, J., et al. 2023, *AJ*, 165, 120
 Kanodia, S., Stefansson, G., Cañas, C. I., et al. 2021, *AJ*, 162, 135
 Kempton, E. M. R., Bean, J. L., Louie, D. R., et al. 2018, *PASP*, 130, 114401
 Kotani, T., Tamura, M., Nishikawa, J., et al. 2018, *Proc. SPIE*, 10702, 107021I
 Mahadevan, S., Ramsey, L., Bender, C., et al. 2012, *Proc. SPIE*, 8446, 84461S
 Mahadevan, S., Ramsey, L. W., Terrien, R., et al. 2014, *Proc. SPIE*, 9147, 91471G
 Mandel, K., & Agol, E. 2002, *ApJL*, 580, L171
 Mann, A. W., Dupuy, T., Kraus, A. L., et al. 2019, *ApJ*, 871, 63
 Mercer, A., & Stamatellos, D. 2020, *A&A*, 633, A116
 Murray, C. A., Delrez, L., Pedersen, P. P., et al. 2020, *MNRAS*, 495, 2446
 Narita, N., Fukui, A., Kusakabe, N., et al. 2015, *JATIS*, 1, 045001
 Narita, N., Fukui, A., Kusakabe, N., et al. 2019, *JATIS*, 5, 015001
 Narita, N., Fukui, A., Yamamuro, T., et al. 2020, *Proc. SPIE*, 11447, 114475K
 NASA Exoplanet Archive 2023, Planetary Systems, vVersion: 2023-06-22 14:16, NExSci-Caltech/IPAC
 Parviainen, H., Palle, E., Zapatero-Osorio, M. R., et al. 2020, *A&A*, 633, A28
 Parviainen, H., Palle, E., Zapatero-Osorio, M. R., et al. 2021, *A&A*, 645, A16
 Pass, E. K., Winters, J. G., Charbonneau, D., et al. 2023, *AJ*, 166, 11
 Paxton, B., Bildsten, L., Dotter, A., et al. 2011, *ApJS*, 192, 3
 Paxton, B., Cantiello, M., Arras, P., et al. 2013, *ApJS*, 208, 4
 Paxton, B., Marchant, P., Schwab, J., et al. 2015, *ApJS*, 220, 15
 Quirrenbach, A., Amado, P. J., Caballero, J. A., et al. 2014, *Proc. SPIE*, 9147, 91471F
 Reiners, A., Zechmeister, M., Caballero, J. A., et al. 2018, *A&A*, 612, A49
 Ricker, G. R., Winn, J. N., Vanderspek, R., et al. 2015, *JATIS*, 1, 014003
 Sabotta, S., Schlecker, M., Chaturvedi, P., et al. 2021, *A&A*, 653, A114
 Sanchis-Ojeda, R., & Winn, J. N. 2011, *ApJ*, 743, 61
 Schlieder, J. E., Gonzales, E. J., Ciardi, D. R., et al. 2021, *FrASS*, 8, 63
 Schwab, C., Rakich, A., Gong, Q., et al. 2016, *Proc. SPIE*, 9908, 99087H
 Scott, N. J., Howell, S. B., Gnilka, C. L., et al. 2021, *FrASS*, 8, 138
 Sebastian, D., Gillon, M., Ducrot, E., et al. 2021, *A&A*, 645, A100
 Skrutskie, M. F., Cutri, R. M., Stiening, R., et al. 2006, *AJ*, 131, 1163
 Smith, J. C., Stumpe, M. C., Van Cleve, J. E., et al. 2012, *PASP*, 124, 1000
 Southworth, J., Wheatley, P. J., & Sams, G. 2007, *MNRAS*, 379, L11
 Stefansson, G., Cañas, C., Wisniewski, J., et al. 2020, *AJ*, 159, 100
 Strakhov, I. A., Safonov, B. S., & Cheryasov, D. V. 2023, *AstBu*, 78, 235
 Stumpe, M. C., Smith, J. C., Catanzarite, J. H., et al. 2014, *PASP*, 126, 100
 Stumpe, M. C., Smith, J. C., Van Cleve, J. E., et al. 2012, *PASP*, 124, 985
 Tamura, M., Suto, H., Nishikawa, J., et al. 2012, *Proc. SPIE*, 8446, 84461T
 Tayar, J., Claytor, Z. R., Huber, D., & van Saders, J. 2022, *ApJ*, 927, 31
 Thorngren, D. P., Fortney, J. J., Murray-Clay, R. A., & Lopez, E. D. 2016, *ApJ*, 831, 64
 Torres, G., Bakos, G. Á., Kovács, G., et al. 2007, *ApJL*, 666, L121
 Vogt, S. S., Allen, S. L., Bigelow, B. C., et al. 1994, *Proc. SPIE*, 2198, 362
 Yee, S. W., Petigura, E. A., & von Braun, K. 2017, *ApJ*, 836, 77
 Zacharias, N., Finch, C. T., Girard, T. M., et al. 2013, *AJ*, 145, 44